# Experimental studies of water intercalation in a layered silicate system

Simen Berg Lutnæs

February 15, 1999

# Acknowledgements

Several people have helped me during the work with my thesis. Some of them must be mentionned specifically.

First of all my supervisor, Jon Otto Fossum, has contributed considerably with ideas, suggestions and valuable hints. His experience as an experimental physicist, knowledge in the field of soft condensed matter and capability to encourage and motivate has impressed me from the beginning.

Professor Emil J. Samuelsen and Knut Aasmundstveit guided me safely through the different x-ray techniques, answering willingly all my questions.

Jon Samseth and Arvid Ødegård Jensen have helped me out with everything concerning Small Angle Neutron Scattering, and I am very thankful for their contribution.

Ph.D. Guillaume Manificat, my room-mate and french inspirator, has helped me picking the right words with the right spellings.

I would like to thank my mother Grethe, my father Trond and my brothers Ola and Sverre for being there when I need them.

Finally, I would like to thank my wife Elin for reading and correcting some of the errors in the text and for her daily support and invaluable assistance in my every day life.

Trondheim 02.14.99

Simen Berg Lutnæs

# Summary

This work is primarily an experimental study of a layered, synthetic silicate system. The material under study has been Fluorhectorite $Li(Mg_2Li)Si_4O_{10}F_2$, purchased from Coring, US. Three different experimental techniques have been utilized in order to relate the microscopic and the macroscopic properties of the material. Interlayer cations have been exchanged with $Na^+, K^+$ and $Ni^{2+}$ to investigate the interlayer cations' influence on the behaviour of the material. A procedure to make a dry, synthetic clay sample is established. Temperature and relative humidity have been varied within the range of $20 - 80°$C and 4% to 97% at a temperature of 25°C while measuring. X-ray diffraction patterns show intercalation of one monolayer of water in dry clay samples, and simulations have been done that fit the experimental data. Rocking scans indicate possible amelioration of the crystallite alignment when water is intercalated in the structure of the material. Small Angle Neutron Scattering (SANS) on dry clay samples and humid clay samples has been performed as well as SANS on clay powder with different cations present. The data analysis indicates a possible self-similar surface fractal $D$ in the range of $2,1 < D < 2,7$. Continuous Wave ultrasonics on nickel fluorhectorite shows significant anisotropy in the material. An effective elastic modulus as a function of humidity is proposed, but further data analysis must be done to draw valid conclusions. Furthermore, the swelling of the clay material is recorded in two directions. Apparently, the material expands only in one direction, along the surface normal of the clay platelets, when water enters the material.

The experimental work required to acquire the data in this work, combined with the amount of information to be analysed within the time limit of four months surpasses my capacity. Therefore, this report must be regarded as a fundament for further data analysis and possible valid conclusions.

# Contents

# Chapter 1

# Introduction and motivation

*"It is better to be vaguely correct than precisely wrong"*
*Amartya Sen, Nobel laureate in economics, 1998*

Solid-state physicists and chemists have studied the properties of several intercalation compounds extensively over the past several decades [1]. One general class of host materials which can form a wide range of intercalation compounds has until recently received little attention from the solid state community. This new "class" of materials is that which includes aluminosilicate clays (often called sheet silicate clays). Much of the current understanding of the basic structure and properties of clay minerals is the result of early work by soil scientists and mineralogists. A typical example is an article by R. Garcia et al. [2], treating clay minerals from antique pottery. People from the oil industry have also become interested in the understanding of clays as a material, because borehole instability in shales is regarded as a major technological problem area in oil and gas well drilling [3]. Theoretical works including eg. non-linear Boltzman theory for swollen clays [4], and simulations of compaction of assemblies of platelike particles [5, 6] has been done quite recently. These particle systems seem to be very interesting for several physicists around the world for the moment.

This work is primarely an experimental contribution to the understanding of a synthetic clay, namely the fluorhectorite. Some earlier studies has been done on this material eg. Kaviratna et al. [7]. To understand the basic physical properties of clays as a material requires a clean and well defined system if valid conclusions are to be drawn. These systems can only be found in synthetic materials where the chemistry and the structures are regular and considered known. The important parameters controlling the intercalation behaviour of clay systems are humidity and temperature. Wada et al. [8] have studied the intercalation of water in vermiculite and they have established a map shown in figure 1.1 of the different states in the material that

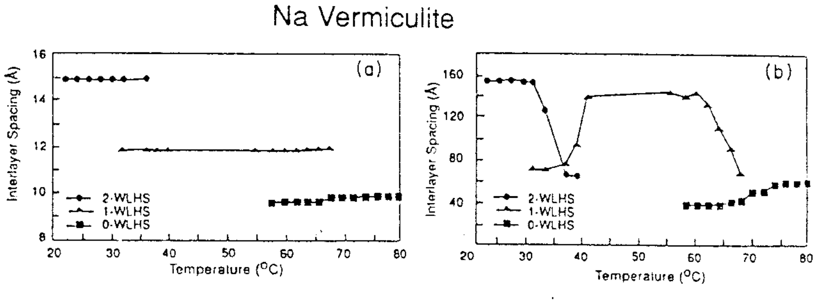

Figure 1.1: Stepwise dehydration of water in vermiculite. Taken from [8]

illustrates the fascinating phenomenon of intercalation. The material hosts zero-, one- or two monolayers of water depending on the temperature and the humidity. A similar behaviour is expected for fluorhectorite, and this work will hopefully be a contribution for further understanding of the intercalation of water in fluorhectorite.

# Chapter 2

# Theory

In the first part of this chapter, a brief description of intercalation compounds and some of the properties of clays in general will be given. A focus is hold on the specific properties of fluorhectorite. Furthermore, some basic expressions in the nomenclature of the field of clay physics will be clearified. Fluorhectorite has been studied by means of three different experimental techniques, namely Small Angle Neutron Scattering (SANS), X-ray diffraction and a Continuous Wave ultrasound technique. Without ambitions of giving a thourough discussion of the theory behind all these techniques, it is important to give the reader a brief introduction and some references for further readings.

## 2.1 Intercalation compounds

Intercalation compounds generally consists of porous host structures which can ingest a variety of guest species into the pore spaces with litle or no distortion of the host structure itself [9]. These layered solids have been grouped into three classes according to the rigidity of their layers with respect to distortions involving atomic displacements transverse to the layer plane [10]. Class I contains only two compounds, graphite and boron nitride. Examples of class II materials are layer dichalcogenidessuch as $TiS_2$ and metal chlorides such as $FeCl_2$ and $CoCl_2$. Class II materials present a stiffer structure than the layers of class I solids. The prototype of class III materials are the layered silicate clays [11], like fluorhectorite. Because the clay layers are many atoms thick, they will be quite "rigid" against transverse layer distortions. In fact the clay layers are so rigid that they can be propped apart or pillared by widely spaced intercalants. For further readings on the rigidity of intercalated solids, see Y. Cai et al. [12].

## 2.2 Clay minerals

For a complete introduction to different types of clays, their structure and chemical compositions, the works of B. Velde [13] or H. van Olphen [14] are recommended. The following description of clays as a material is primarily based on their work. Natural clay minerals are the smallest physical structures in geology. Clays were initially defined as consisting of grains less than $2\mu$m in diameter, beyond the limit of microscopic resolution. This was a definition of the nineteenth century, which had only microscopic means of investigation. Wentworth´s scale, seen in figure 2.1, commonly used in North America, gives names to the different structures in geology depending on their size. Apart from their grain size, clays do also have a mineral structure in common. Geologists say that most clays in natural settings have a **phyllosilicate** or sheet structure. There are other minerals of different grain shapes present in the clay fraction like zeolites, quartz and oxide minerals, but most geologists think of sheet silicates when speaking of clay minerals.

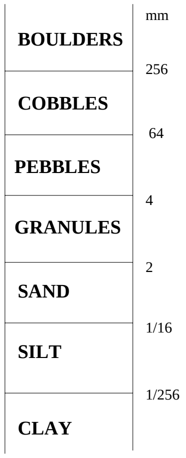

Figure 2.1: Wentworths scale

### 2.2.1 Smectites

The most important property of some clay minerals is the capacity to change volume by absorbing water molecules or other polar liquids into their structure: The swelling property. Clays are divided into **swelling** and **non-swelling** type minerals. Swelling clays are called **smectites**. Several types of non-swelling clays exist. Depending on their structure and chemical composition, they are classified as illites, chlorites, kaolinites, sepiolite-palygorskites etc. However, this work focuses on one single type of smectite, consequently the subject of non-swelling clays is left without any further descriptions.

### 2.2.2 Chemical structure

There are three fundamental molecular units involved in the sheet structure of a smectite: A tetrahedron, an octahedral polyhedron and an interlayer cation. The tetrahedron, seen in figure 2.2, consists of one silicon atom surrounded by four oxygen anions. This is the most basic unit of the clay structure. The silicon tetrahedral arrangements are linked one to another by highly covalent bonding through sharing of oxygens atoms, seen in figure 2.3. The interlinked oxygens are called basal oxygens, wereas on the opposite end of the linked tetrahedra, one finds the apical oxygens. These apical oxygens are shared with other series of cations, situated inside the octahedrally coordinated cation polyhedron, shown in figure 2.4. The octahedral cations are coordinated with six oxygens or hydroxyl units, and they are interlinked with the tetrahedral sheet cations through the apical oxygens of the silica tetrahedra. The cations found in the tetrahedrally coordinated sheets are principally $Si^{4+}$. Some substitutions of $Al^{3+}$ is common, and occasionally $Fe^{3+}$ is present. Cations found in the octahedrally coordinated layer are

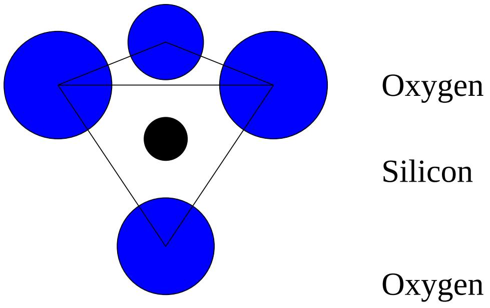

Figure 2.2: Tetrahedron, basic unit of the clay structure

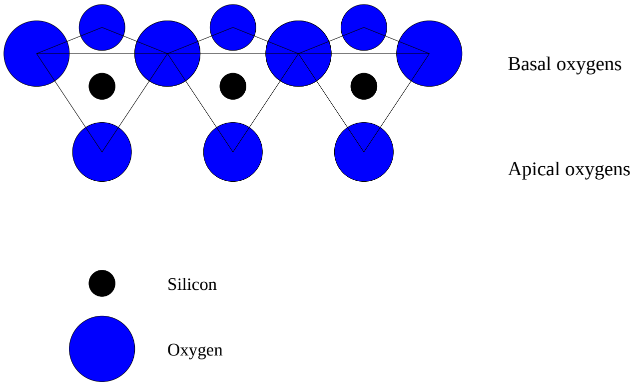

Figure 2.3: Interlinked tetrahedrons

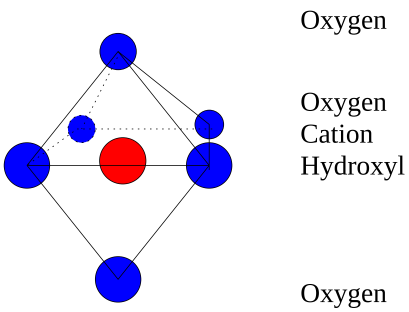

Figure 2.4: Octahedreally coordinated cation polyhedron

more varied in species: $Al$, $Mg$ *and* $Fe^{2+}$ are the principal species, but $Fe^{3+}$, $Ti$, $Ni$, $Zn$, $Cr$, $Mn$, and $Li$ can also be present. Different cations will give different names to the clays. The hydroxyl anionic units can be replaced to a certain extent in some clay structures by $F$ or $Cl$ anions. This is certainly the case for the fluorhectorite, where all the $OH$-groups have been replaced by $F$. Furthermore, fluorhectorite originates from the substitution of $Li^+$ for $Mg^{2+}$ in the octahedral layer [7]. The octahedrally coordinated layer is sandwiched between two tetrahedrally coordinated sheets, and this arangement is called a **2:1 structure**. Finally, fluorhectorite is called a trioctahedral smectite. This means that all of the three possible sites in the octahedrally coordinated layer are filled. Figure 2.5 is a 2-dimensional drawing of the fluorhectorite structure.

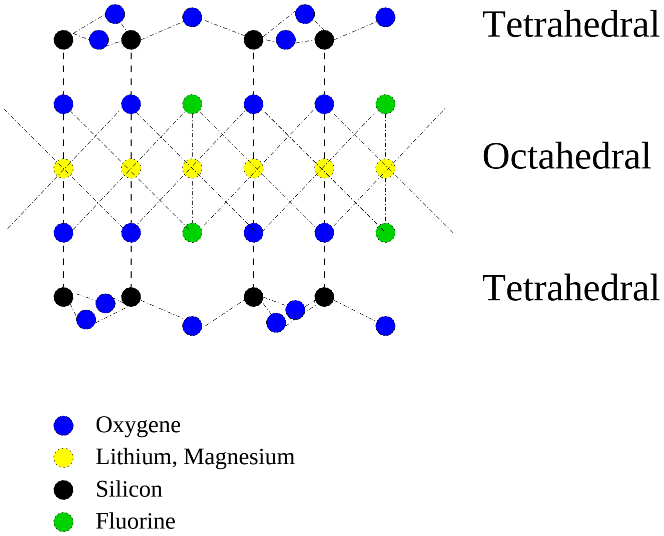

Figure 2.5: Two dimensional drawing of fluorhectorite structure

### 2.2.3 Interlayer cation

Cation substitutions in the sheet structure, for example trivalent ion substituted for $Si^{4+}$ in the tetrahedral site, create charge imbalance in the layer. While the edges of the sheets are positively charged due to the crystal structure, the surfaces become negatively charged. The charge imbalance is compensated by inserting cations into the hexgonal holes in the basal oxygen layer. The sheets in figure 2.6, bonded through interlayer compensating cations, are stacked upon one another to form a three dimensional crystal like the one in figure 2.7 The sheets are held firmly together by cations attracted into the holes in the oxygen array.

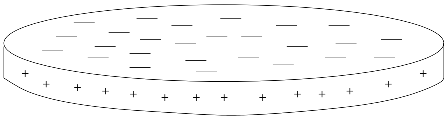

Figure 2.6: Single sheet of smectite clay

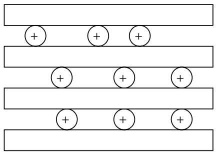

Figure 2.7: Pile of smectite sheets with interlayer cations

### 2.2.4 d-spacing of clay sheets

The characteristic distance between the sheets in figure 2.7 is called the d-spacing. This distance is dependent on how the interlayer cations are organized between the sheets, and if there are any host molecules like water intercalated in the structure. A 3D-drawing of a smectite is given in figure 2.8. The d-spacing distance is specified in the figure

### 2.2.5 Interlayer cation exchange

The swelling process observed when smectites are immersed in an aqueous solution is the result of a mixture of different forces between charged clay platelets and the influence of chemical equilibrium in the solution. This complex picture of forces involves several phenomenons at different length scales. A reference to the book of J. Israelachvilli [15] is given for an overview. However, depending on the clay concentration in the solution, the particle size

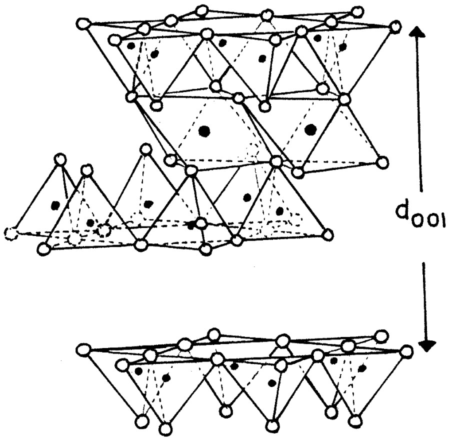

Figure 2.8: 3D smectite with d-spacing specified. Taken from Solin & Lee [16]

distribution and the layer charges of the sheets, the final state of the swelling process is platelets randomly oriented in the solution (IL) containing free cations. See for example the phase diagram of montmorillonite in figure 2.9. By adding a proper amount of salt to this solution, it is possible to exchange

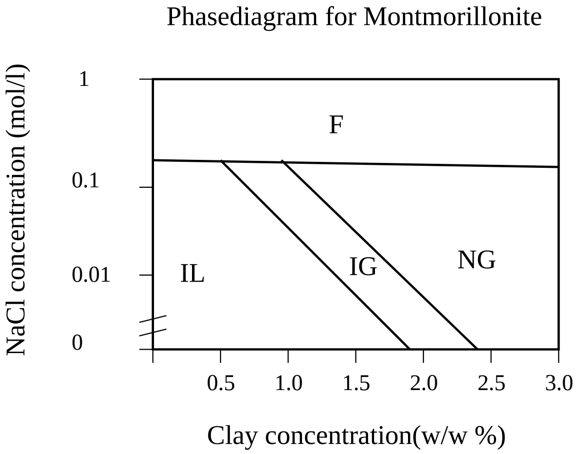

Figure 2.9: Sketch of phasediagram montmorillonite taken from Gabriel et al. [17]

the original interlayer cations with the cations of the salt. This operation is done to homogenize the species of ions present in natural smectites, or to study different swelling properties of synthetical smectites like fluorhectorite. A standard procedure for this treatment is given in the chapter dedicated to experiments.

## 2.3 Diffraction

Two of the experimental techniques utilized in this work are scattering of x-rays and scattering of neutrons. These techniques are widely used to reveal the atomic structure, size, dynamics and shape of colloidal systems. The principles of these techniques are very much the same. However, some major differences have to be mentioned:

- The energy of each particle.
  - A photon with a wavelength of 0.15 nm has an energy that is 200.000 times greater than a neutron of the same wavelength.
- The different ways of scattering:
  - X-rays are scattered by electrons in the material.
  - Neutrons are scattered by the nuclei in the material.
- The penetration depth in the material
  - Neutrons penetrate much deeper into the material because they are scattered by the nuclei

Even though they represent an important part of this work, it would be too ambitious to present the mathematical formalism that is common for both of them. A classical approach would not describe the scattering correctly, and introducing quantum electro-magnetic theory would be out of this work's scope. The interested reader can read the book of Stephen W. Lovesey [18]. However, a popular explanation of why scattering patterns occur in neutron- and in x-ray scattering is appropriate. This presentation is based on the introduction book in the molecular biophysics course at NTNU, Trondheim [19], and the textbook of H. P. Klug & L. E. Alexander, called *X-ray diffraction procedures* [20].

### Particle-wave duality

It is well known that appropriate experiments confront us with a complementary behaviour of photons and neutrons that are both particles and waves. These two properties are not found to be in contradiction because it is not possible to devise a single experiment that tests both particle and wave aspects at once. X-rays can be described as photon-particles with energies of kilo-electron-volt order, but also as electromagnetic radiation-waves. We benefit from the wave-like property of neutrons and photons when performing diffraction and scattering experiments.

### 2.3.1 Mathematical description

Due to their wave-like properties, the mathematical formalism describing the total scattering of an ensemble of physical objects is basically the same for a flux of photons and a flux of neutrons. The measured intensity from a scattering experiment on a system of N physical objects can very roughly be presented like this: First, the contributions from every single volume element $d^3r$ in object number $i$ is integrated over the total volume of object number $i$. Then, we make a summation of all the objects to find the total intensity. A clay sample constitutes such an ensemble of physical objects. If we go down to the level of the scattering objects, knowing that they constitute points in a regular lattice given by the chemical structure, some situations are easily found where the intensity of the scattered beam must has a maximum value. The criterium for an intensity maximum is called the Bragg criterium.

### 2.3.2 Quasi-elastic scattering

When photons or neutrons are scattered against atoms in a material, some small amount of the incomming particles' linear momentums are transferred to the atoms. In our case this loss of energy is considered to be so small that the energy, and hereby the wavelengths of the incoming and the scattered radiation are approximatly the same. Hence, the magnitude of the incoming and the scattered wavevector, $\vec{k}_{in}$ and $\vec{k}_{out}$, can be considered to be conserved. This scattering is referred to as **quasi-elastic** scattering. Figure 2.10 shows a wavevector being scattered by an object. The scattering vector, $\vec{q}$, is defined:

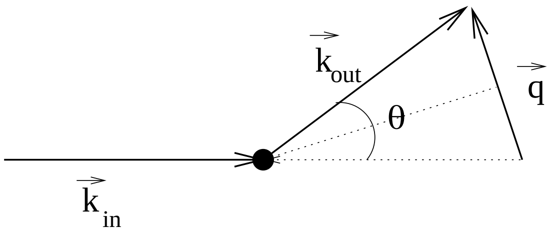

Figure 2.10: Quasi-elastic scattering

$$\Delta\vec{k} = \vec{k}_{out} - \vec{k}_{in} = \vec{q} \tag{2.1}$$

and this vector is an important parameter that constitutes a basis for the data analysis for the experimental techniques. For quasi-elastic scattering, $|\vec{k}_{in}| = |\vec{k}_{out}| = |\vec{k}| = k = \frac{2\pi}{\lambda}$.

### 2.3.3 Photons and x-ray radiation

A photon flux can be represented by a harmonic, continuous *real wave*, with a wave number $k_p$, given by:

$$k_p = \frac{2\pi}{\lambda_p} = \frac{2\pi\nu_p}{c} \tag{2.2}$$

where $\lambda_p$ is the wavelength of the electromagnetic radiation, $c$ is the velocity of the wave and $\nu_p$ is the frequency. X-rays are usually produced by the sudden deceleration of fast moving particles. Electrons from a glowing filament (the catode) are accelerated through vacuum by a voltage, usually from 15 to 60 kV, and they strike a metal target (the anode). Within the target the electrons encounter crowds of other electrons, which causes a sudden deceleration. The result is X-radiation of two major varieties shown in figure 2.11. One form has a broad continuous spectrum of wavelengths, and the other one has very sharp peaks of discrete wavelenghts characteristic of the target material. The characteristic wavelengths of the anode material appear because the accelerated electrons possess sufficient energy to knock certain anode electrons out of their orbital. This leaves vacancies that are immediately filled by electrons from higher energy levels. The energy lost in the drop appears as a photon with frequency $\nu_p$. The relation between the wavelength $\lambda_p$ and the frequency $\nu_p$ is well known for electromagnetic radiation and given in equation 2.3:

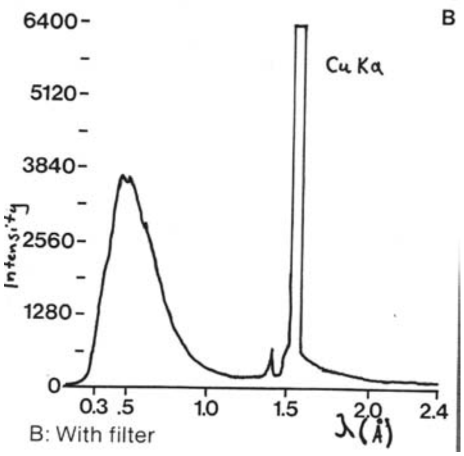

Figure 2.11: Intensity as a function of wavelength for a copper anode. Cu $K_\beta$ is removed with a filter. Taken from a poster by Siemens

$$\lambda_p = \frac{c}{\nu_p} \tag{2.3}$$

The energy difference between orbitals is a function of the number of protons in the nucleus and is therefore different for every element. Another aspect is that an incident electromagnetic wave interacts with the charged electrons in the material to be analysed. The electrons vibrate in resonance with the electromagnetic wave and hereby become emitters of electromagnetic radiation.

### 2.3.4 Bragg criterium for x-rays

In an x-ray scattering experiment, at least two different modes are possible. In transmission mode the x-ray beam penetrates the sample and the intesity of the signal is detected on the opposite side of the sample. In reflection mode, the intensity of the reflected signal is detected. In the latter case, the geometric situation is like the one in figure 2.12. The path difference between diffracted photons (a) and (m) is $AB + BC = 2d \sin\theta$. When the path difference is equal to an integer times the wavelength $\lambda_p$ of the photon, we will observe a distinct peak in the measured intensity. This is Bragg's law. In terms of $\vec{q}$, figure 2.13 illustrates the same situation. With the scattering angle $2\theta$ defined in the figure, it is easily seen that:

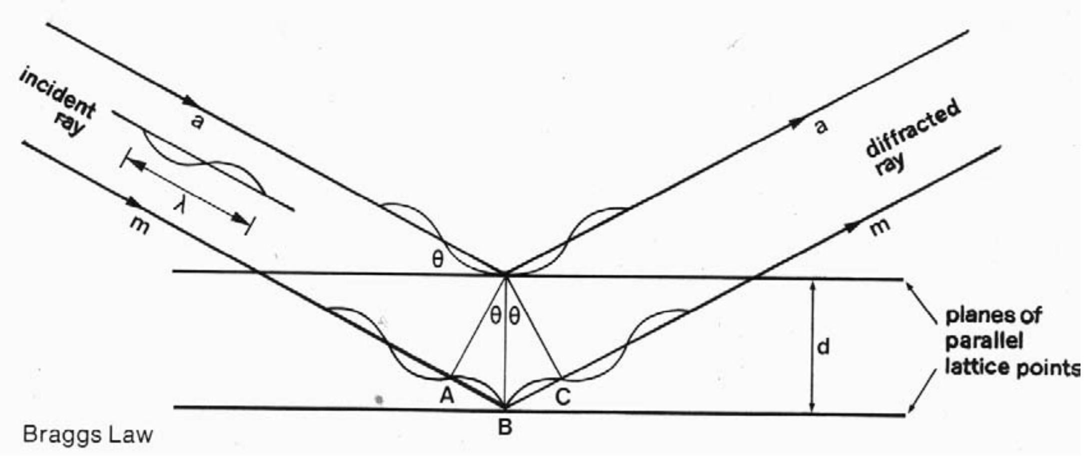

Figure 2.12: Reflection mode in x-ray scattering. Taken from a poster by Siemens

$$q = |\vec{q}| = 2k \sin\theta = \frac{4\pi}{\lambda} \sin\theta \tag{2.4}$$

Inserted into Bragg's law, substituting for $\sin\theta$:

$$d = \frac{2\pi n}{q} \tag{2.5}$$

Intensity plotted as a function of q will thus reveal directly the d spacing in the clay structure for the (001) peak.

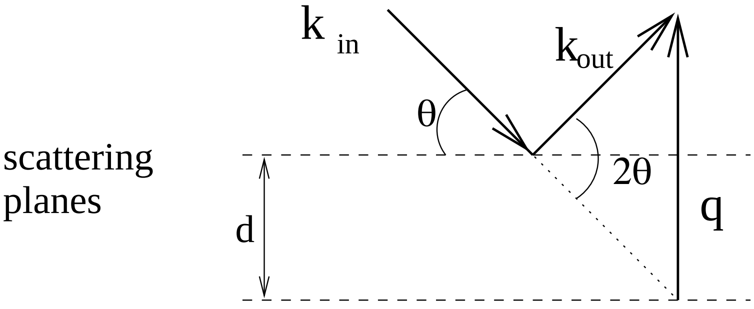

Figure 2.13: $\vec{q}$ for x-rays reflection

### 2.3.5 Contributors to the intensity

Bragg's law is the first approach to model nature, but some simplifying assumptions were made when deriving it:

- The incident beam is perfectly monochromatic
- The rays are perfectly parallel
- The rows of atoms are perfectly ordered and part of a perfect, infinite crystal
- The crystal is perfectly oriented for diffraction to occur.

Real circumstances differ from the idealized ones. This introduces some important factors that we need to include in the data analysis. Thorough work has been done for several years to understand the diffraction pattern from clay systems. Theory for such analyses in *X-Ray Diffraction and the Identification and Analysis of Clay Minerals* by Moore & Reynolds [21]. When analysing the diffraction patterns from a clay sample, information about the sample is found both from the positions of the peaks and their shapes. The 2 circle diffractometer we used had a peak width at half height of about 0.5deg $2\theta$. Peaks wider than 0.5deg $2\theta$ will therefore give valuable information about the sample. A characteristic of all clay minerals is imperfection in their crystal order because of their small crystal size. These small crystals cause noticeable line-broadening. Considering the scattering planes, the diffraction peaks get narrower with increasing order, due to cancellations. The total scattered intensity is basically a product of three different contributions.

### Layer scattering factor

The layer scattering factor $G(\theta)$, represents the scattering efficiency of the unit cell. $G(\theta)$ is given by:

$$G(\theta) = \sum_n P_n f_n \cos(\frac{4\pi z_n \sin\theta}{\lambda_p}) \tag{2.6}$$

where $\theta$ is the angle given in figure 2.13, $P_n$ is the number of atoms of type $P$ per atomic layer, $f_n$ is their scattering power and $z_n$ is the displacement of the atomic layer, in Ångstrøms, from the center of symmetry measured along a line normal to the (00l)plane. The intensity , measured by the detector, is equal to $|G(\theta)|^2$. $G(\theta)$ is a differs for each clay type, see Cole et al. [22]. However, we found the graph, seen in figure 2.14, of $G(\theta)$ for trioctahedral silicates in Brindley & Brown [23]. The graph was digitalized and $2\theta$ was substituted with $q$. $G(q)^2$ was plotted and three gaussians were fit to the function in Origin, as shown in figure 2.15. This function, with different parameters, will be used to fit the measured intensities from x-ray data aquired in the laboratory.

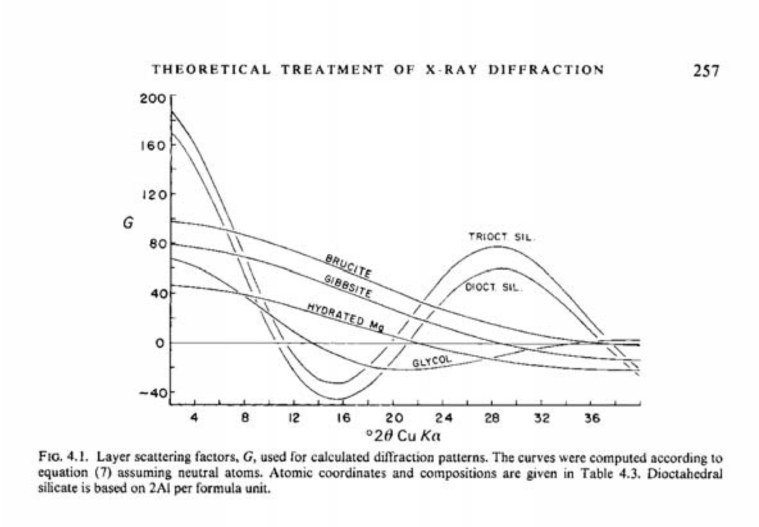

THEORETICAL TREATMENT OF X-RAY DIFFRACTION 257

FIG. 4.1. Layer scattering factors, G, used for calculated diffraction patterns. The curves were computed according to equation (7) assuming neutral atoms. Atomic coordinates and compositions are given in Table 4.3. Dioctahedral silicate is based on 2Al per formula unit.

Figure 2.14: Graph of $G(\theta)$ taken from [23]

### Interference function

The three-layered crystal structure of the clay sheets already discussed, creates an additional scattering adjacent to the $hkl$-diffraction peak positions, and even in small amounts in between these positions [23]. Calculations of

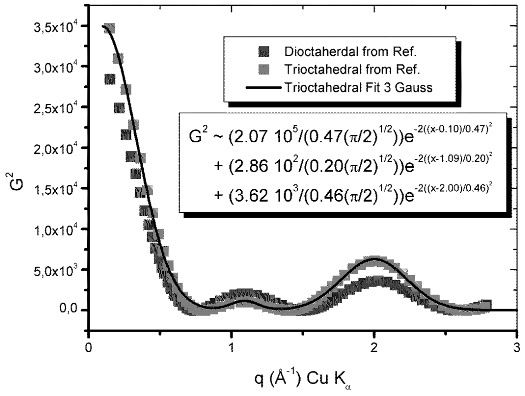

Figure 2.15: $G(q)^2$ fitted to three Gaussian functions

the diffraction pattern for any assemblage of such cells, including this additional scattering is called the interference function, and given the label $\Phi$. The interference function is continuous function and given by:

$$\Phi(\theta) = \frac{\sin^2(\frac{2\pi N D \sin\theta}{\lambda_p})}{sin^2(\frac{2\pi D \sin\theta}{\lambda_p})} \tag{2.7}$$

where N is the number of unit cells stacked in coherent scattering array along the z-axis and D is the d-spacing in the z direction. Substituting $\sin\theta$ from equation 2.4 relates the interference function with $q$. The calculation of the interference function assumes that the d-spacing is uniform in every crystallite. For swelling clays this may not be the case. Imagine that a clay sample is partially intercallated with one and two monolayers of water respectively. This situation was treated mathematically by Hendicks & Teller, and the expression is given in equation 2.8.

$$\Phi = \frac{2P_A P_B \sin^2(\frac{2\pi\sin\theta(D_A - D_B)}{\lambda_p})}{1 - 2P_A P_B \sin^2(\frac{2\pi\sin\theta(D_A - D_B)}{\lambda_p}) - P_A\cos(\frac{2\pi\sin\theta D_A}{\lambda_p}) - P_B\cos(\frac{2\pi\sin\theta D_B}{\lambda_p})} \tag{2.8}$$

$P_A$ and $P_B$ refer to proportion of species A and B of unit cell thickness $D_A$ and $D_B$ respectively. $P_A + P_B = 1$. In the chapter for results and data analysis, an effort will be done to decide whether the data should be fitted to the ordinary interference function or to the Hendicks-Teller function.

### Lorentz-Polarization factors

The last factor considered is a combination of two effects dependent on $\theta$. The first effect is a polarization factor that accounts for increases in the peak an the background scattering from a maximum at 0deg $2\theta$ to a minimum at 90deg$2\theta$. The basis for this change is that as radiation comes from the tube it is unpolarized, but the scattering causes a degree of polarization related to the angle between the incident and the diffracted beams. The total energy of the scattered beam is proportional to the factor $\frac{1+\cos^2 2\theta}{2}$. The second effect is called the Lorentz factor and is a combination of two geometrical factors.

- One term handles the volume of the increment of the crystal that is exposed to primary irradiation
- One term relates the number of crystals favorably oriented for diffraction at any Bragg angle $\theta$

When those terms are combined, the Lorentz-polarization factor for single crystals is:

$$L_p = \frac{1+\cos^2 2\theta}{\sin 2\theta} \tag{2.9}$$

Using the relation between $\theta$ and $q$ from equation 2.4, we can now derive:

$$L_p = \frac{1+\cos^2 2\theta}{\sin 2\theta} \approx \frac{4\pi}{q\lambda_p} \tag{2.10}$$

for small q.

### Graphical summary

The total intensity in the 00l diffraction pattern as a function of $q$ is calculated from the expression:

$$I(\theta) = [G^2(\theta)][\Phi(\theta)][L_p(\theta)] \tag{2.11}$$

Figure 2.16 shows graphically the contributions from the different factors for different $2\theta$, and how they form the total intensity pattern in figure 2.17. The mathematical expression for the total intensity for different q-values is established, and the different parameters are manipulated to find out whether we are dealing with a pure Bragg- or a Hendricks-Teller situation. These studies are presented in the chapter dedicated to results and data analysis.

## 2.3.6 Neutron scattering

A neutron flux can be represented by a harmonic, continous and *complex wave* with a wave number $k_n$ given by:

$$k_n = \frac{2\pi}{\lambda_n} \tag{2.12}$$

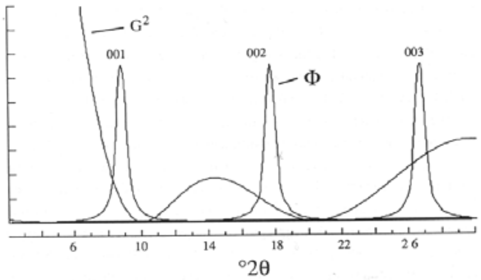

Fig. 3.15. Interference function (Φ) for N = 2-15, d(001) = 10 Å, and $G^2(\theta)$ for an illite unit cell.

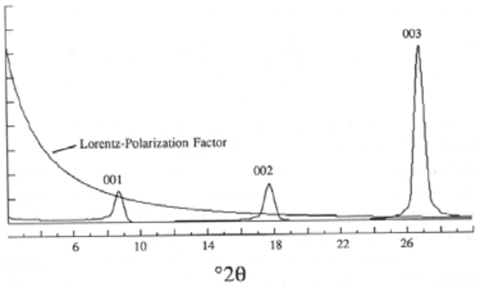

Fig. 3.16 The Lorentz-polarization factor and the product of $G^2$ and Φ.

Figure 2.16: Sketch taken from Moore & Reynolds [21]

where $\lambda_n$ is the **de Broglie**[1] wavelength of the neutron, given by:

$$\lambda_n = \frac{h}{p_n} \tag{2.13}$$

Here, $h$ is Planck's[2] constant and $p_n$ is the linear momentum of the neutron.

There are two means of producing neutrons in sufficient quantities for worthwhile experiments. One approach to neutron production is the one used in spallation neutron sources where intense, high-energy proton beams are generated in particle accelerators and synchrotrons and then directed at a target of heavy nuclei. The other, and more obvious approach used in this thesis, is to get neutrons from a nuclear reactor. In this technique, neutrons are released by the fission of uranium-235. Each fission event releases 2-3 neutrons, though one of these is needed to sustain the chain reaction. The best neutron source in Scandinavia is the DR-3 reactor at Risø Research Center, Denmark. The neutrons do interact with the nuclei of the material to be analysed. Each nucleus of the material represents a scatterer. This

---

[1] Louis de Broglie, French physicist (1892-1987), Nobel laureate in physics, 1929

[2] Max Planck, German physicist (1858-1947), Nobel laureate in physics, 1918

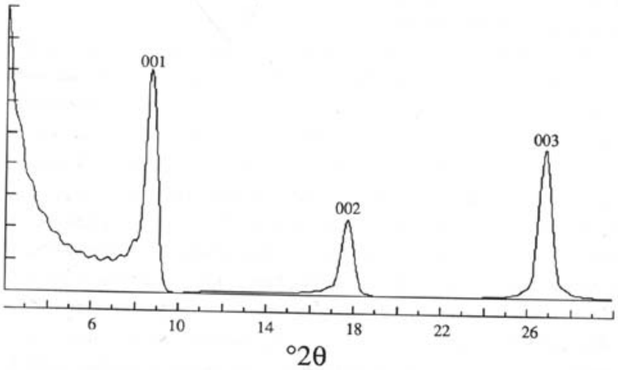

Fig. 3.17. Calculated diffraction patterns for illite, N= 2 - 15.

Figure 2.17: Total intensity pattern. Taken from Moore & Reynolds [21]

implicates a much higher penetration depth in the material for neutrons as compared to the one for photons.

### 2.3.7 Bragg criterium for neutrons

In a neutron scattering experiment, the scattering angle $\theta$ is defined as in figure 2.10. From this figure, it is seen:

$$|\vec{q}| = q = \frac{4\pi}{\lambda} \sin\frac{\theta}{2} \tag{2.14}$$

For $\theta$ small, a good approximation is:

$$q = \frac{2\pi}{\lambda} \sin\theta \tag{2.15}$$

By a simple trigonometric argumentation, we find the criterium for an intensity maximum for the pile of clay-sheets in figure 2.18. The difference in pathlength, $\Delta s$, for the two trajectoires is given by:

$$\Delta s = d \sin\theta \tag{2.16}$$

When $\Delta s$ is equal to an integer times the incident wavelength $\lambda_n$, we will get an intensity maximum. This intensity maximum is also called a Braggpeak. Substituting for $\sin\theta$, we get the relation between the layer separation $d$ and $q$, given in equation 2.17.

$$d = \frac{2\pi n}{q} \tag{2.17}$$

This relationship is independent of the wavelength $\lambda_n$, and the same as for x-ray scattering. It is very useful when comparing data obtained with different wavelengths. Different wavelenghts are very common in neutron scattering.

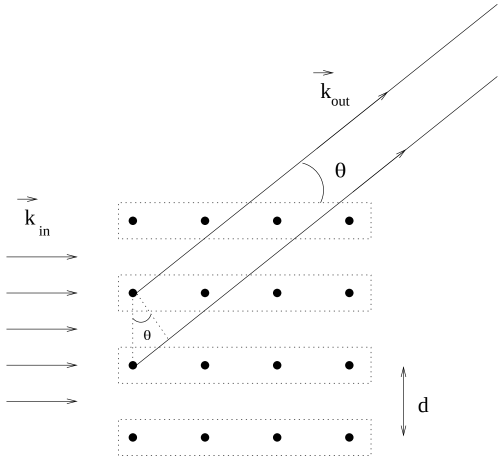

Figure 2.18: Braggpeak criterium for neutron scattering on clay sheets

### 2.3.8 Microgeometry studied by Small Angle Neutron Scattering

SANS is a technique that makes it possible to study the microgeometry of different samples. In the simplest model, one can view the clay as a two phase system. A random interface separates the pore space and the particle space. Two studies in the mid-80s [24, 25] suggest that the pore-grain interface in rocks is described by self-similar fractals with nonuniversal dimensions ($2 \leq D \leq 3$). Po-zen-Wong & James Howard [27] studied by means of SANS three types of sedimentary rocks (sandstones, shales and carbonates). In order to reveal a fractal behaviour of the interface between pores space and grain space. Their study is based on the following theory:

For small wave vector q, the neutrons see the neutrons see the rock as a simple two-phase system. In the first Born approximation [18], the scattering cross section, $I(q)$ is simply proportional to the Fourier transform of the geometric correlation function [28]. For self-similar fractals, this leads to a non-integer power law behaviour in the scattering:

$$I(q) = Aq^{-\alpha} + B \tag{2.18}$$

where $B$ represents the incoherent background. If the volume (or mass) of the scatterer is a fractal, then $\alpha = D$ [29, 30]. If only the surface is a fractal, then $\alpha = 6 - D$ [30, 31]. Since $D \leq 3$ and $6 - D \geq 3$, surface fractals and volume fractals are readily distinguished.

## 2.4 Continuous Wave ultrasonics

The fundamental quantities measured in a cw[3] ultrasonic experiment are the attenuation (absorption) and phase velocity of the ultrasonic wave. According to Mason [32], a cw transmission spectrometer can be broken down into three sections:

- a transmitter section
- a composite resonator assembly
- a receiver section

Figure 2.19 shows a sketch of the different devices in a cw setup. The ultrasonic composite resonator consists of the specimen under study, opposite faces of which have been ground optically flat and parallel, together with two suitably affixed transducers. The cw-technique relies on the establishment of ultrasonic standing waves in the composite resonator. Each of the standing wave resonances is characterized by a resonant frequency $\omega_m$ and a quality factor defined by:

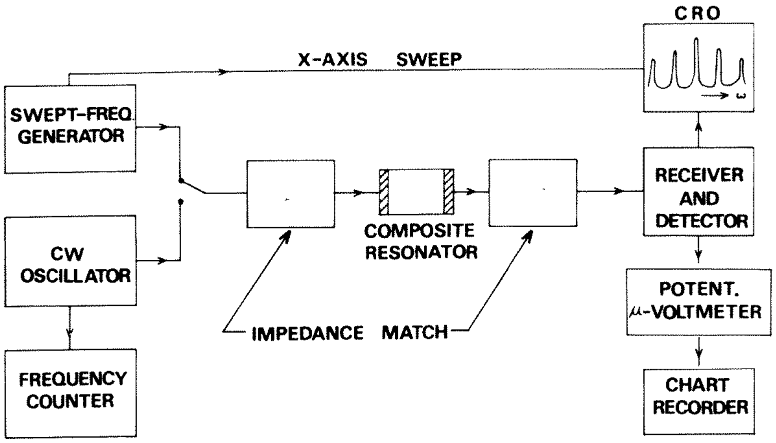

Figure 2.19: Required devices for cw ultrasonics. Taken from [32]

$$Q \equiv \frac{\omega_m}{\Delta\omega_m} \tag{2.19}$$

where $\Delta\omega$ is the linewidth at the half power points. $Q$ is related to the ultrasonic attenuation, and in the limiting case of a one dimensional, isolated resonator in which plane waves are propagated, $Q = \frac{\omega_m}{2\omega_\alpha}$, where $\omega_\alpha$ is the utrasonic attenuation in radians per second. In our case, the relation between the ultrasonic attenuation and the $Q$-factor is a little bit more complicated.

---

[3] cw: continuous wave

It will be out of the scope of the present works limit dicussing these problems here. The priority is the relationship between the acoustic phase velocity in the sample and the observed mechanical resonance frequencies $\omega_m^c$ of the composite resonator. The composite resonator consists, as already mentioned, of two transducers and one sample. The sample and the transducers can be represented by a transmission-line equivalent circuit. Equivalent Electrical Circuit theory [32] and [33] gives an expression for the frequency of the $m^{th}$ mechanical resonance of the sample and the frequency separation between half-wave resonances of the sample, $\omega^s$ in terms of the observed composite resonator resonance frequencies, $\omega^c$.

$$(\omega_{m+1}^s - \omega_m^s) = (\omega_{m+1}^c - \omega_m^c)(1 + 2\eta) \tag{2.20}$$

where

$$\eta = \frac{\rho_t l_t}{\rho_s l_s} \tag{2.21}$$

$\rho_t$ and $\rho_s$ being the density of transducer and sample respectively and $l_t$ and $l_s$ are their lengths. In our case, $\eta \ll 1 \Rightarrow$ the term is neglected. The phase acoustic velocity is found from equivalent circuit theory to be:

$$v_s = \frac{(\omega_{m+1}^s - \omega_m^s) l_s}{\pi} = 2l_s(f_{m+1} - f_m) \tag{2.22}$$

Knowing the length of the sample, $l_s$ and measuring the distances between the mechanical resonant frequencies will give us the acoustic phase velocity of the sample. The acoustic phase velocity is related to the effective elastic moduli $C_{eff}$ according to the usual expression:

$$C_{eff} = \rho v^2 \tag{2.23}$$

where $\rho$ is the mass density of the material and $v$ is the acoustic p-wave velocity in the material. For further readings on cw ultrasonic measurements and the damping capacity of layered materials, see Jin [34] and Brandner [35].

### 2.4.1 Elastic moduli of Fluorhectorite

An increase or decrease in the acoustic phase velocity will certainly be an indicator of a changing, effective elastic moduli, $C_{eff}$. However, on the microscale, the number of independent elastic moduli depends on the crystallographic structure of the material. According to Brindley et al. [23], the sepiolite-resembling fluorhectorite has a preferred space group: monoclinic $\frac{C2}{m}$. L. E. McNeil et al. [36] have studied the elastic moduli of muscovite mica by means of Brillouin scattering. Muscovite mica represents the same monoclinic structure as the structure supposed for fluorhectorite. The monoclinic symmetry of their material requires 13 independent elastic moduli: $C_{11}, C_{22}, C_{33}, C_{44}, C_{55}, C_{66}, C_{12}, C_{13}, C_{15}, C_{23}, C_{25}, C_{35}$ and $C_{46}$. McNeil claims that out of these, $C_{11}, C_{22}, C_{66}$ and $C_{12}$ are primarily dependent on the bondings within the layers. The remaining moduli are governed by the weaker interlayer bonding and should be more sensitive to perturbations caused by temperature, pressure, intercalation and the like. In a cw ultrasonic experiment, these moduli would represent the change in the acoustic sound propagation.

## 2.5 Humidity

It is important to control the humidity in the atmosphere around the sample while measuring. In the laboratory setting, it is most convenient to control the relative humidity in the air. However, the absolute humidity in the air is the important parameter. Therefore, the difference between realtive and absolute humidity will be specified in order to avoid potential misunderstandings.

### 2.5.1 Absolute vs relative humidity

Relative humidity is the the ratio between the water contents of the air and the water contents in saturated air at the same temperature. Absolute humidity is $[\frac{g}{m^3}]$ of water in the air. The relation between relative and absolute humidity at different temperatures is given in figure 2.20. At a constant temperature it is possible to keep the absolute humidity at a constant value.

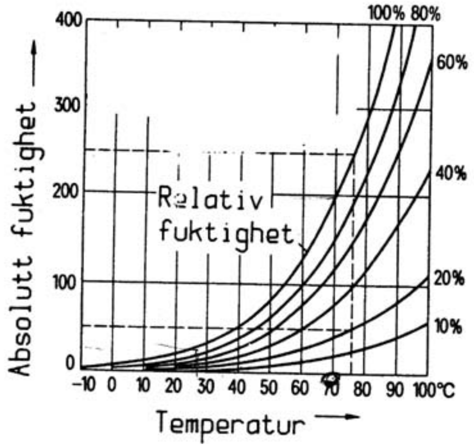

Figure 2.20: Relative- and absolute humidity at different temperatures. Taken from [37]

Table 2.1: Saturated salt solutions with their respective vapor pressures

| Salt | Amount: $\frac{g}{100cm^3water}$ | Rel. humidity at $T = 20°C$ |
|---|---|---|
| Silica Gel($SiO_2$) | — | 4 |
| Sodium Chloride ($NaCl$) | 35.7 | 76 |
| Potassium Chloride ($KCl$) | 34.7 | 86 |
| Potassium Sulphate ($K_2SO_4$) | 12 | 97 |

### 2.5.2 Saturated salt concentrations

The vapor pressure above saturated salt in water solutions can be found in Handbook of chemistry and physics. It is highly dependent on the type of salt dissolved in the solution. Table 2.1 gives some examples of the relative humidity obtained in air forced through the solution by a pump. For further reading on vapor pressures, see Bailar et al. [26].

# Chapter 3

# Experiments

Three different experimental techniques have been chosen in order to reveal some properties of a dry clay system and its interaction with water molecules. This chapter contains a receipt on how the sample preparation was done, and how the experiments were performed.

## 3.1 Sample preparation

It is important to work with a clean, synthetic clay system because it enables us to control as many physical parameters as possible in the material. The experiments have been performed on dry samples of **lithium fluorhectorite** purchased from Coring US. The chemical formula for this synthetic hectorite is: $Li(Mg_2Li)Si_4O_{10}F_2$. It is a strongly swelling smectite. We chose this specific clay because earlier studies [38] had shown that it was possible to make dry and thick samples of it, without major problems. Li-fluorhectorite comes from Coring as a clay-powder. The powder grains are sub-$mm$-sized and they consist of several clay platelets that can be separeted into individual clay particles when dissolved in water. The sample preparation follows this procedure:

- Dissolving clay powder in distilled water
- Exchange interlayer cations
- Drying of clay samples

Each point in the procedure will be discussed with an emphasis on important aspects.

### 3.1.1 Dissolving in water

Clay powder is mixed in pH-adjusted distilled water in order to separate the clay crstallites into single platelets. pH is adjusted to 10 with NaOH and

KOH alternately in order to avoid the possibillity that $Mg^{2+}$-ions will leave their positions in the octahedral layer of the clay sheet. This effect is observed experimentally by Butterworth & Thompson [39] in 1991 and Levitz et al. [40] in 1997 for a long-term gelation of laponite. This may also be the case for fluorhectorite. When these ions leave their positions in the clay sheet, the structure of the sheet may be perturbated, and we do not know whether we are working with nice, flat sheets or with buckled ones. The change of chemical structure may introduce new effects in the measurements which are impossible to trace back to its origin. For this reason, the work is done with sheets keeping their chemical structure intact.

### Phase diagram

Clay-water-salt systems usually have rich phase diagrams. No proper phase diagram for lithium-fluorhectorite cab be found in the literature, and establishing it is not the topic of this work. However, continuous comparision with the phase diagram of montmorillonite and laponite[1] in figure 3.1 shows a possible lack of the gel-phase for fluorhectorite. Pictures have been taken of different concentrations of salt and fluorhectorite in water, fig.3.2. The contents of the samples 1-6 in the figure is given in table 3.1.1. It is clearly seen from the picture that even in the sample without salt, the particles will sediment. This may be a result of the particle size, meaning the fluorhectorite particles are no longer brownian, but it can also be a result of the layer charge of fluorhectorite. Kaviratna et al. [7] have listed the physical properties of three smectites: laponite, montmorillonite and fluorhectorite. The numbers are given in table 3.1.1. The three different clay types all have a density of $2,8\frac{g}{cm^3}$. If the particles are assumed to be disks and the diameter of fluorohectorite particles is 20000Å, then montmorillonite particles are $10^{-2}$. Furthermore, the higher charge density of fluorhectorite results in a

Table 3.1: Fluorhectorite sample contents

| Sample No. | w% clay | Molarity |
|---|---|---|
| 1 | 10 | 0 |
| 2 | 1,4940 | $10^{-2}$ |
| 3 | 0,2507 | $10^{-2}$ |
| 4 | 2,9850 | $10^{-3}$ |
| 5 | 1,4751 | $10^{-3}$ |
| 6 | 0,2485 | $10^{-3}$ |

---

[1] Synthetic hectorite with similar chemical structure

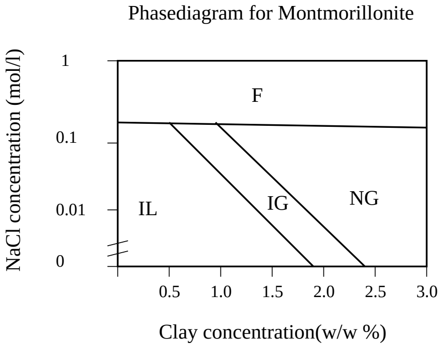

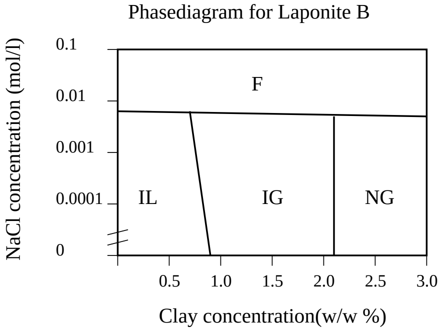

Figure 3.1: Sketch of phasediagram for laponite B and montmorillonite taken from Gabriel et al. [17]

higher number of cations present in the solution. Hence, Debye's screening length, given in equation 3.1, gets smaller.

$$\kappa = \left(\frac{\sum_i \rho_{\infty i} e^2 z_i^2}{\epsilon k T}\right)^{\frac{1}{2}} m^{-1} \tag{3.1}$$

Here, $\rho_{\infty,i}$ is the number density of ion $i$ in the bulk, $z_i$ is the valence of electrolyte number $i$, $\epsilon$ is the electric permitivity for the solvent ( $\epsilon = \epsilon_0 \epsilon_r$ ), $k$ is Boltzmann's constant and $T$ is the absolute temperature. For a further introduction to forces between charged platelets in a solvent, see Intermolecular & Surface Forces by J. Israelachvilli [15]. If we take a closer look at sample No. 4 in figure 3.3, we see four distinct layers in the suspension. This is common for samples with a salt concentration of $10^{-3}\frac{moles}{liter}$. There is a water phase at the top. The smallest particles form aggregates that do not sediment. There are two such layers of aggregates. At the bottom, we find the heaviest particles that probably have sedimented. One conclusion of this interesting observation is that the fluorhectorite particles constitute a polydisperse system. The biggest particles have sedimented and the others form different aggregates that probably are involved in a sedimentation equi-

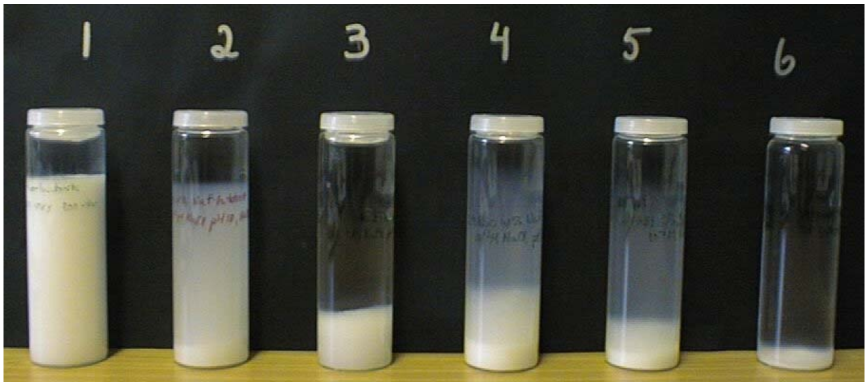

Figure 3.2: 6 samples of fluorhectorite in water and NaCl

Table 3.2: Fluorhectorite sample contents

| Clay | Particle size (Å) | Charge density ($\frac{e^{-1}}{unitcell}$) |
|---|---|---|
| Laponite | 200 | 0,4 |
| Montmorillonite | 2000 | 0,6 |
| Fluorhectorite | 2000-20000 | 1,2 |

librium. Interestingly enough, one can imagine this vertical phase transitions as the x-axis in the phasediagram in figure 3.1. The highest clay concentration is at the bottom of the glass and a much lower clay concentration is at the top. This indicates that the phase diagam is a function of particlesize. The size distribution and the charge density of the fluorhectorite particles are both factors that may result in flocculation and sedimentation without further addition of salt. More accurate studies have to be carried out to understand this behaviour, and the differences between the phase diagrams for the different hectorites. In this specific case, it could be interesting to follow the hight of the different phases as a function of salt concentration and temperature. Furthermore, one could investigate the different transitions with light-scattering techniques.

### 3.1.2 Cation exchange

When dissolved and continuously stirred for 24 hours, different salts were added to the clay-water suspension in order to exchange the interlayer cations. The amount of salt added is seen in table 3.3 . This quantity was based on the calculations found in appendix B. After two weeks of stirring, the suspen-

Figure 3.3: Fluorhectorite, salt and water with four distinct phases

Table 3.3: Mixture amounts of clay and salt

| Clay | Amount (g) | Salt | Amount (g) | Water (ml) |
|---|---|---|---|---|
| fluorhectorite | 35 | $NiCl_2$ | 50 | 450 |
| fluorhectorite | 35 | $KCl$ | 30 | 500 |
| fluorhectorite | 35 | $NaCl$ | 30 | 500 |

sions were dialysed in pH-adjusted distilled water another two weeks. The dialysis setup is sketched in figure 3.4. The purpose of this treatment was to get rid of excess ions in the suspension. The dialysis water was checked daily for ion contents, using a standard silver-nitrate ($AgNO_3$)-procedure. $AgNO_3$ is added to the dialysis water and formation of $AgCl$ is initiated if $Cl^-$-ions are present in the solution. $AgCl$ is almost insoluble in water and has a white colour. One must be careful when using this procedure in a solution with a pH of 10. This environment allows formation of silverhydroxide that is brown/green. To avoid this formation one must reduce the pH to below 7 with an acid that does not contain $Cl$. We used $H_2SO_4$ to reduce the pH. When there was no sign of $AgCl$ in the dialysis water another $AgCl$-check was done after two days. Still no $AgCl$ in the water means that all the excess ions in the clay suspension are gone and that the cations in the clay suspension are basically the ones coming from the salt. Then the suspensions are ready to dry.

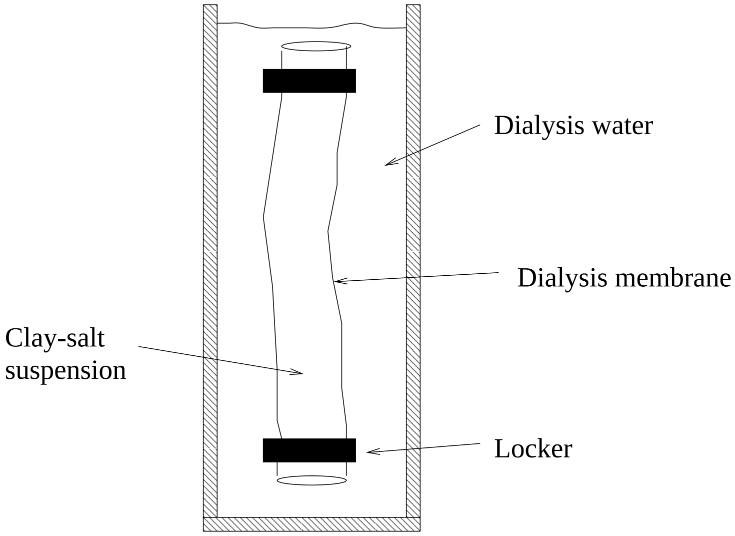

Figure 3.4: Dialysis cylinder setup

### 3.1.3 Drying

The ion-exchanged samples for small angel neutron scattering- and continous wave ultrasonic experiments need to be 2-3 mm thick. Based on previous experiences [38] with the material, a load cell was designed like the one shown in figure 3.5. It allows the clay sample to dry out under a constant uniaxial stress. The stress improves the alignment of the clay particles during drying, as seen in the article by S. A. Solin [9]. The applied load was 500 Newtons and this gives a stress of 120 kPa. Most of the water is pressed

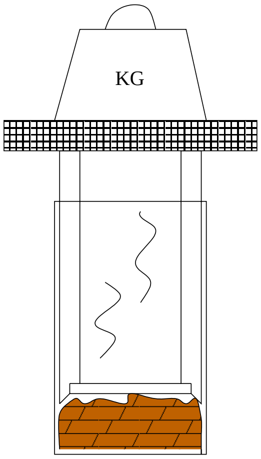

Figure 3.5: Loadcell used for drying clay samples

out in room temperature. Then the load cell is placed in an oven and the temperature is raised to $75^{o}C$. 24 hours later, the sample was taken out of the load cell and stored in the oven without stress. The temperature was raised again to $110^{o}C$ to get out as much water as possible. The final result was cylindrical samples with a thickness of about 5 mm shown in figure 3.6. Samples that are to be studied by x-ray diffraction must be submm. thick in order to perform transmission and reflection $\theta - 2\theta$-scans. These samples were dried in petri dishes under atmospheric conditions.

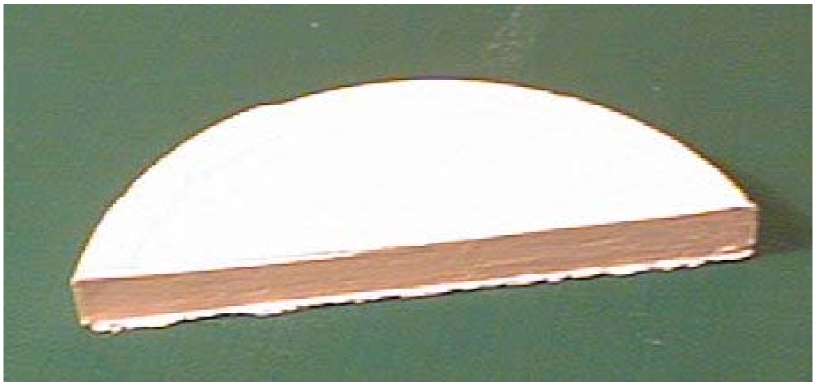

Figure 3.6: Photo of a dried clay sample of fluorhectorite with $K^{+}$-cations

## 3.2 X-ray diffraction

In order to study the intercalation of water in the clay material, I used a 2 circle diffractometer, called Løfte, situated in the laboratory of professor Emil J. Samuelsen at the department of physics, Gløshaugen, NTNU, Trondheim. We made use of its Cu $K_\alpha$ ($\lambda = 1.5418$ Å) rotating anode x-ray source of 8 kW. The radiation is monochromatized by a curved focusing graphite monochromator. The detector is a scintillation counter made by Siemens. A sketch of the instrument is given in figure 3.7. To be able to do measurements on a swelling clay sample, it was necessary to design a chamber where it is possible to control the absolute humidity around the sample and the temperature of the sample. This was done by making a cell like the one in figure 3.8. A tilted "half-moon" of copper is wired with a 25Ω-heater to match the requirements of the temperature controller properly. The temperature controller was a Lakeshore 321 Auto Tuning Temperature Controller.

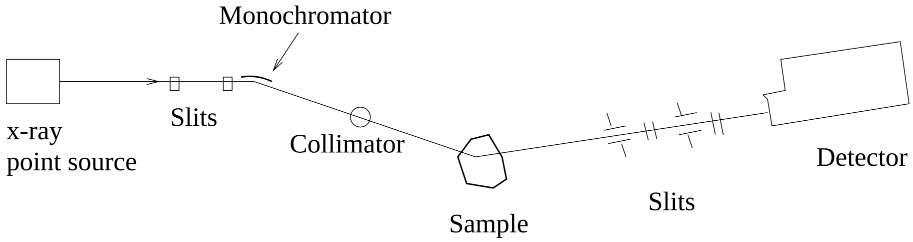

Figure 3.7: Sketch of the beamline in the x-ray diffractometer

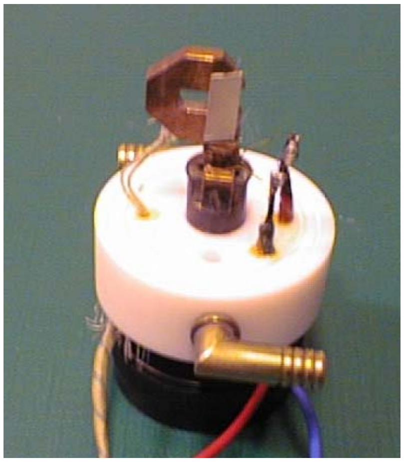

Figure 3.8: Sampleholder for x-ray diffraction measurements on fluorhectorite under a controlled atmosphere

The temperature was measured close to the sample with a copper-konstantan thermocouple. The humidity inside the cell was controlled when pumping air in a closed circle through different salt-solutions, silica-gel and the cell. It was not possible to insert a psychrometer inside the cell to measure the humidity in this setup because it would have disturbed the beamline. However, the volume of the cell is very small (about $60cm^3$) compared to the capacity of the pump (about $1000\frac{cm^3}{minute}$). Therefore, it can be assumed that the humidity inside the cell will be stabilized quickly at the values given in table 2.1. The wall in the cell is a cylindrical, transparent shell of capton. This material does not contribute significantly to the scattering patterns.

### $\theta - 2\theta$ scan

A $\theta - 2\theta$ scan is a well known expression among "x-ray scatterers". I will briefly explain the meaning of this expression for potential "x-ray rookies". $\theta - 2\theta$ scans can be performed in two ways: In a transmission mode and in a reflection mode. In the reflection mode, the situation is the same as the one in figure 3.9. The detector is in the position $2\theta$ from the incident wavevector.

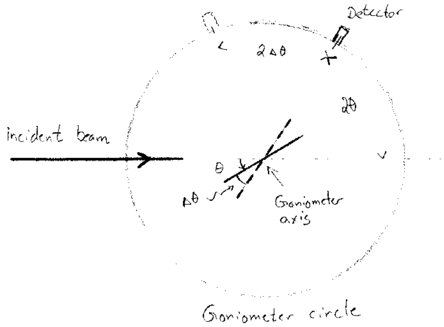

Figure 3.9: $\theta - 2\theta$ scan principle

The sample is rotated an angle $\Delta\theta$ and the detector is simultanously rotated an angle $2\Delta\theta$ to measure the intensity at the position where the signal is strongest.

### 00l-scan

The procedure is the same as for $\theta - 2\theta$ scan. However, a $\theta - 2\theta$ scan is in the real space, while a 00l-scan is in the reciprocal space. Intensity is plotted as a function of $q[\text{Å}^{-1}]$.

### Rocking scan

Clay films are made of tiny crystal fragments or blocks in a nearly parallel alignement as in figure 3.10. A rocking scan is performed to check the orientational distribution of the crystal fragments. Firstly, detector and sample is fixed at a distinct Bragg-peak. Then the detector scans ±20deg while the sample is fixed. The width of the intensity peak is a measure of the alignement of the crystallites. The wider the peak, the more randomly oriented the crystallites are.

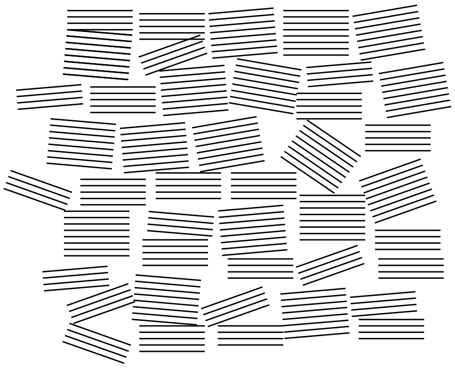

Figure 3.10: Crystal fragments in a clay film

$\theta - 2\theta$-scans were performed in the transmission mode and the reflection mode for the three different cation-exchanged clay systems. To begin with, the ambition was to map the d-spacing (00l) for the three fluorhectorites for temperatures between 25 and 80$^o$C, and relative humidities between 4 and 97% at room temperature. This would have given an informative matrix indicating the stable situations for each clay type. This turned out to be too time consuming, especially when we ran into some problems with the line-up of the instrument. However, during the initial measurements, an interesting phenomenon in the dynamics of the 001- Bragg peak was observed. At a certain temperature and humidity, the peak moved significantly. The movement represents a change in the d-spacing of the sample of about 2.5Å. This is comparable to the size of one layer of water molecules. It was decided to study this developement more thoroughly for the three different clay types. It turned out to be quite different for the three samples. $Ni^{2+}$-samples showed a water adsorption at a higher temperature than $K^+$- and $Na^+$ samples. $K^+$ samples adsorbed water at the lowest temperatures. For the details in this observation, please see the chapter for results and discussion.

## 3.3 Small Angle Neutron Scattering

I brought three different samples of fluorhectorite to the DR3-reactor at Risø, Denmark[2] with respectively $Na^+$, $K^+$ and $Ni^{2+}$ as the interlayer cations. The dry samples had been exposed to temperatures up to $175^oC$ for 6 hours. The scattering was performed along two different directions in the material: Normal and parallel to the expected alignment of the clay particles. Normal direction and parallel direction are defined for an idealized pile of clay sheets in figure 3.11. If we study the criterion for a diffraction peak in the signal, as done in figure 2.18, we see that we can only expect a Braggpeak when the beam is parallel to the particle alignment. No characteristic d-spacing is available for scattering in the normal direction. Mounting the samples on to the sample holders was quite difficult, especially when the samples should be as wide as possible (the beamhole is about 8 mm). This is especially difficult in the parallel direction, but a satisfactory result was obtained with some patience. The photo in figure 3.12 shows the six samples mounted on the sampleholders the way they were measured. The results are given in an own chapter. After some successful measurements were done on the dry samples, we prepared for measurements on $K^+$ and Ni$^{2+}$-treated fluorhectorite with different amounts of water. To carry out these kinds of measurements, you have to put the samples into small quartz cuvettes[3], and it is rather difficult to cut the clay samples to such small pieces without disturbing the alignment of the clay platelets. The samples were cut into pieces by a saw or a scalpel and inserted into the cuvettes as shown in figure 3.13, without major alignment disturbances. The interesting thing to investigate is whether the mean distance between the sheets will change with different ratios of $\frac{D_2O}{hectorite}$. We started out with three different samples and added much $D_2O$ in the first ones. An article of Ramsay et al.[41] about SANS-measurements on hectorite, revealed data of $\frac{D2O}{hectorite}$ up to 10 so we wanted to reach this number in order to see larger platelet separations than we would be able to

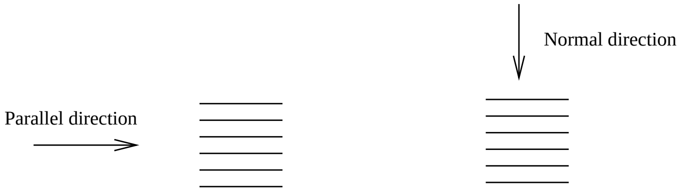

Figure 3.11: Specifications of normal and parallel direction in the particle alignement

---

[2] Information about the DR-3 reactor can be seen at Risø´s homepage on the internet: http://www.risoe.dk/nuk/nukdr3.htm

[3] Uvonic cuvettes, type 21, Pathl: 5mm, code Q

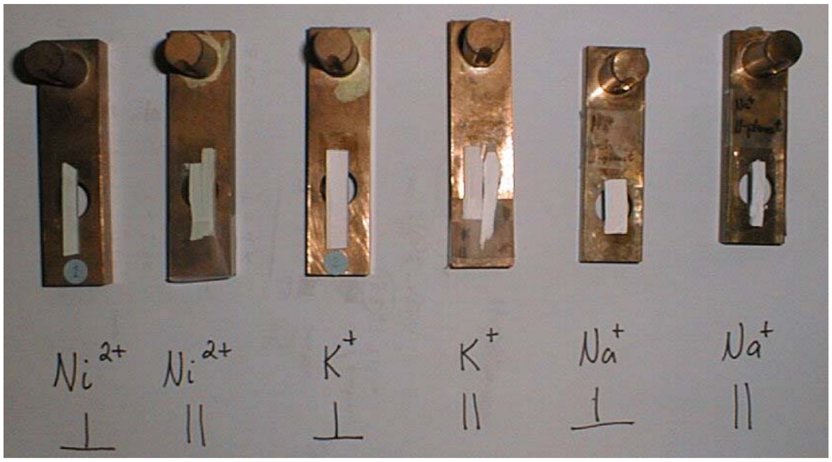

Figure 3.12: Dry clay samples as they were exposed to the neutron beamline

investigate with the x-ray diffractometer. Three samples were made, and it turned out to be too much water for this type of clay. The photo in figure 3.14 shows the samples inside the cuvettes with $D_2O$ present. The samples were allowed to swell for about three hours (maybe not sufficient, but you could at least see the swelling with bare eyes, and some major cracks evolved as well in the material. Air bubbles came out of the dry clay too. These bubbles could probably influence the measurements in a negative way). Because these amounts of $D_2O$ were too large , four new samples were made the same evening with less water. We let them swell for 12 hours. The scans on these four samples, was performed while the temperature in the beam chamber was increasing to about $70^oC$ due to other scans on conducting polymers. Considering the relatively large amount of water inside the clay, we hoped this wouldn't influence the samples, but when we took them out of the beam chamber, lots of water had evapourated from the clay, and made small bubbles on the inside of the cuvettes. Actually, when following the counts on the screen, we could see on the first sample a good anisotropy and a distinct Bragg peak. The second sample started out fine, with the same tendency of anisotropy and Bragg peak, but after some seconds we saw that this peak was continously erased and ended up as a completely noninteresting signal. The effect we saw was most certainly the vapour that started to adsorb on the inner walls of the cuvette and thus disturbed the signal. Therefore, we had to prepare the same samples once again to try to do the scan properly. We started up making new samples with even less water and made four scans on $Ni^{2+}$ and $K^+$ fluorhectorite. These four scans were performed with a temperature of 30°C. Finally, several scans on powder of the three specimens of fluorhectorite were performed.

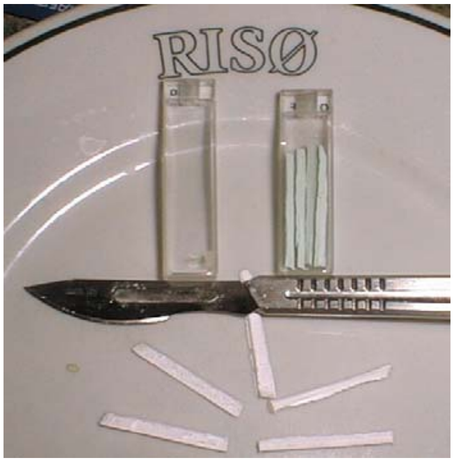

Figure 3.13: Fluorhectorite samples inserted into cuvettes

Figure 3.14: Cuvettes with $D_2O$ and fluorhectorite

## 3.4 Continuous Wave Ultrasonic

Intercalation of water in dry clay samples should intuitively influence the elastic properties of the material. After a characterisation of the material at specific air humidities and temperatures, the focus was moved to a continuous wave ultrasonic technique. The details of this cw-technique is well described in Mason & Thurston [42]. The apparatus used in this study is described in an article by O. M. Nes et al. [43], and the experimental principle is sketched in figure 3.15. Piezoelectric p-wave- and s-wave transducers made by Panametrics were used. The s-wave results are not commented in this report. Both wavemode transducers had a center frequency of 5 MHz. To control the humidity and the temperature around the sample, the cw-apparatus was placed inside a chamber designed for this purpose during my project work [38].

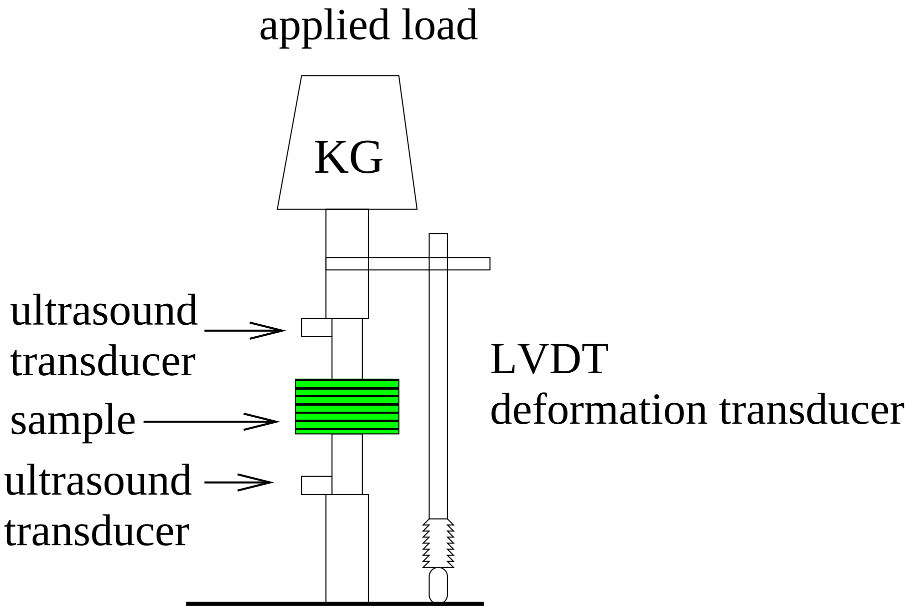

Figure 3.15: Experimental setup for CW ultrasonics

### 3.4.1 Deformation measurements

Three LVDT[4]-transducers are used to measure the deformation in the clay sample during humidification. The sample was under a constant uniaxial stress of 520kPa when swelling. The signal from the transducers were read continuously by a DaQ PC-lab1200 card from National Instruments. LVDT-

---

[4] Linear Variable Differential Transformer

transducers and instrumentation were delivered by RDP Electronics[5] Ltd. We calibrated the transducers separately using four plugs with defined dimensions. The signals are averaged over 50 measurements in order to reduce the effect of minor fluctuations. Results are shown in table 3.4.1.

Table 3.4: LVDT calibration

| Length (mm) | Transducer 1(V) | Transducer 2(V) | Transducer 3(V) |
|---|---|---|---|
| 0 | 0,022 | 0,083 | 0,063 |
| 0,48 | 0,962 | 1,104 | 1,157 |
| 1,06 | 2,378 | 2,415 | 2,598 |
| 1,56 | 3,679 | 3,62 | 3,818 |

A scatterplot in Origin together with a linear regression curve:

$$Y = A + B * X \tag{3.2}$$

is found in figure 3.16 for transducer 3. The slope of the regression curves are the same for the three transducers. When $\Delta\epsilon_z$ symbolize the vertical deformation in mm, the relation between measured voltage, $V$, and deformation is found to be

$$\Delta\epsilon_z = 0.41 \Delta V \tag{3.3}$$

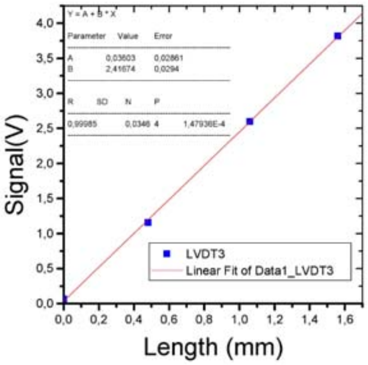

Figure 3.16: Calibration curve for LVDT-transducer 3

---

[5] LVDT-specifications listed in appendix

This relation will become important when analysing the LVDT data.

### 3.4.2 Temperature

To be able to control the temperature in the range of $20 - 80^oC$ on the clay sample, a peltier-element was used as a heater and a Pt-100 element was used to to measure the temperature. The Pt-100 element was connected to a 1mA constant current source[6] and the voltage across the resistor was continuously read by a commercial National Instruments DAQ Card[7]. The temperature/resistance relationship of a platinum resistance thermometer like this is given in equation 3.4 for temperatures between $0^oC$ and $850^oC$.

$$R_t = R_0[1 + 3.9083 * 10^{-3}t] \tag{3.4}$$

Here $R_t$ is the resistance at a temperature $t$ in $^oC$ and $R_0$ is the resistance at $0^oC$. $R_0$ must be calibrated in ice water if the Pt-100 element is uncalibrated. The peltier element was sandwiched between two copper plates. One of these copper plates was held at a constant temperature and the other plate transferred heat to the sample holder. This plate was greased with thermogrease and designed to fit the sample holder like a glove. This is seen in figure 3.17. The Pt-100 element was inserted in a hole in the warm copperplate about 2 cm from the sample. This is not an ideal solution for an exact reading of the temperature of the sample. However, we "calibrated" the system once, using another Pt-100 element as a substitute for the sample. The temperature difference between the sample position and the position 2 cm away varied , of

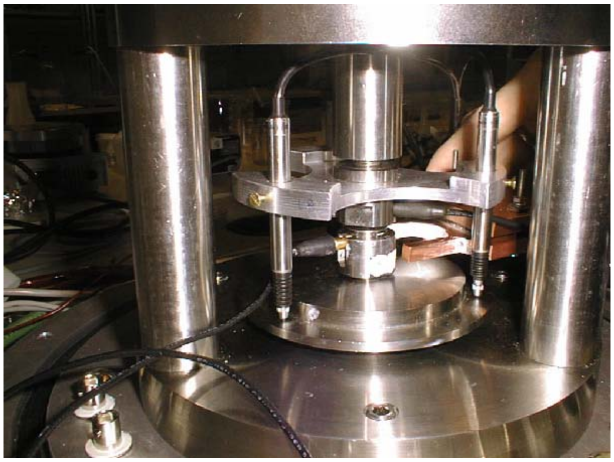

Figure 3.17: Sample holder and copperplate greased with thermogrease

---

[6] Made by Elektronikkverkstedet, NTNU, Trondheim

[7] Lab-PC-1200

course, with the temperature. Nevertheless, the difference was never beyond $5^oC$. A better way to measure the temperature of the sample would be to use a thermocouple glued directly onto the sample, but we did not have one at our disposal at that time. The transducer rig is made of stainless steel and has a mass of about 20 kg. Consequently, the peltier element had problems delivering the effect needed to reach a temperature of $80^oC$. The maximum temperature we obtained was $65^oC$ at the sample position. In order to reach a temperature of $80^oC$, it is necessary to use a heater like the one on the x-ray sample holder. Furthermore, better thermal isolation of the transducer holders can be done, preventing the heat to "leak" away from the sample. The temperature of the sample was controlled by a PID-regulator made in LabView. I used the PID-solution proposed by LabView as the basis for my program. However, with the 1mA constant current source, the 12-bit resolution of the DaQ Card in the range of 0-10 volts was not satisfactory to get a presice reading. To examplify this; given an $R_0$ in equation 3.4 of $100\Omega$ a $1^oC$-change of temperature is a change in resistance of $0.39\Omega$. When connected to a constant current of 1mA, and studying Ohm's law in equation 3.5

$$U = RI \tag{3.5}$$

we see that the $1^oC$-change of temperature equals a change in voltage of $3.9 * 10^{-4}$. A 12-bit resolution of a range from 0-10 volts is :

$$\frac{10}{4096} = 2.44 * 10^{-3} \frac{Volts}{bit} \tag{3.6}$$

Hence, noise in the signal resulting in a change of one bit equals a temperature of more than $6^oC$. This is not a satisfactory situation if we want to control the temperature accurately. To average out the noise in the signal used by the PID regulator, we modified the PID-regulator in LabView. The program code is unfortunately not included in this document due to problems including the code in appendix. The code can be seen by asking research scientist Jon Otto Fossum[8]. The signal is an average over the last 100 readings and it gives the PID regulator a smoother input than the original solution. However, one must be aware that this procedure conseals an important problem in the temperature reading accuracy. One has to come up with a better arrangement to control the temperature precisely on the sample. The important aspects are:

- Better thermal connection between sample and thermometer
- More stable signal from the thermometer, matching the resolution of our DaQ-card

---

[8] fossumj@phys.ntnu.no

# Chapter 4

# Results and discussion

This chapter is divided in three sections. All the results from the laboratories are presented and discussed. An emphasis will be made on x-ray data, because the amount of questions and different aspects linked to the different observations are too numerous to be analysed within the thesis period of four months.

## 4.1 X-ray results

Before the results are presented, the resolution function for the apparatus is shown in figure 4.1. The resolution function is found in the manual for the x-ray apparatus [44]. Peaks more narrow than q=0,03 do not give information about the sample. It is seen from the figure that stacks with more than 17 sheets will give narrower peaks than the resolution function. The figures and plots are presented systematically for each ion type.

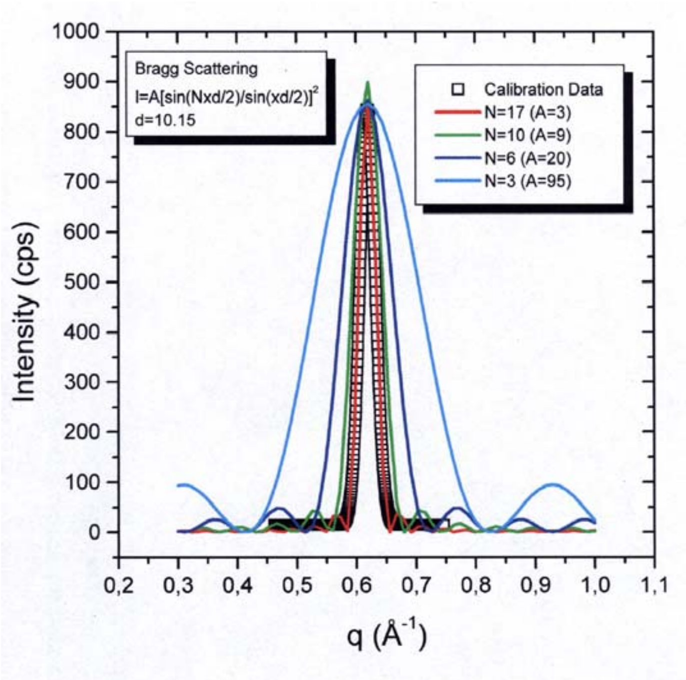

Figure 4.1: Resolution function of x-ray apparatus with simulated braggpatterns for different numbers of sheets N, in a crystallite

### 4.1.1 Wet and dry clay for total q range

Wet samples are measured at a temperature of $25°C$ and relative humidity of 97% at a temperature of $25°C$. Dry samples are measured at a temperature of $80°C$ and a relative humidity of 4% at a temperature of $25°C$. The total q range is $0,4 < q < 2,4$.

#### Nickel Fluorhectorite

The figures show a movement in the (001) posistion. The movement represents a dimension comparable with the dimension of one water molecule. Possible (00l)-positions are suggested in the figures. The (001)-peak is proposed based on findings in the literature [23]. The d-spacing is found from the well-known formula: $d = \frac{2\pi n}{q}$. Some peaks in the diffraction pattern are not well understood for the time being. However, simulations of the diffraction pattern later in this chapter fits the measured intensities satisfactorily.

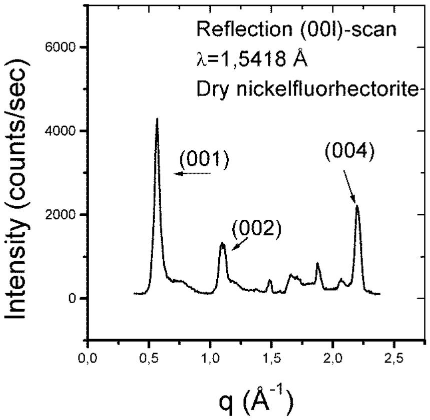

Figure 4.2: Nickel fluorhectorite at dry conditions

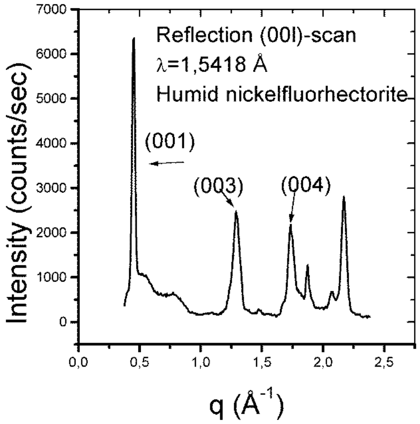

Figure 4.3: Nickel fluorhectorite at wet conditions

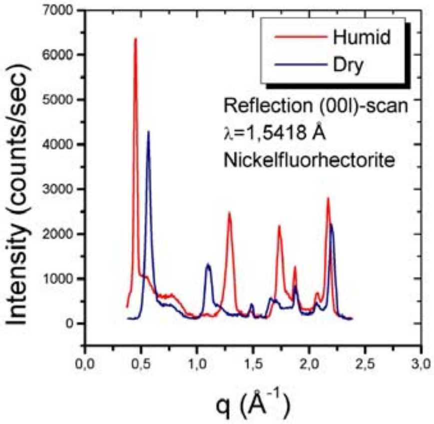

Figure 4.4: Previous figures in the same plot

### Sodium Fluorhectorite

The figures show a movement in the (001) posistion. This movement represents a dimension comparable with the dimension of one water molecule. Sodium fluorhectorite shows a similar behavior to nickel fluorhectorite. One monolayer of water is most probably intercalated in the sheet structure.

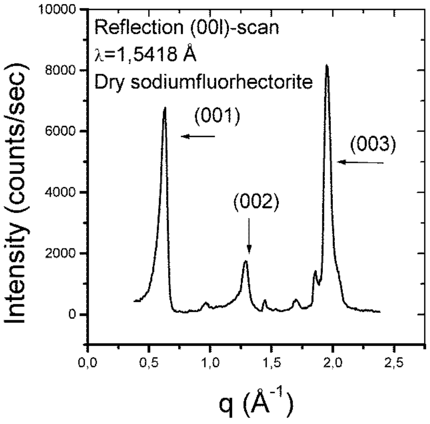

Figure 4.5: Sodium fluorhectorite at dry conditions

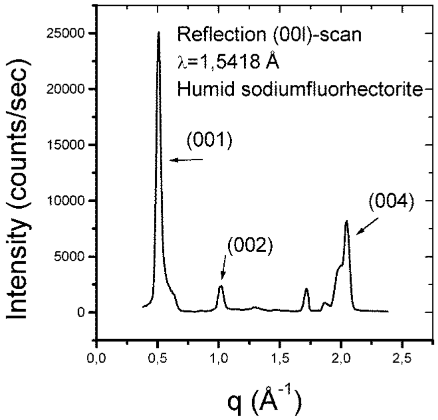

Figure 4.6: Sodium fluorhectorite at wet conditions

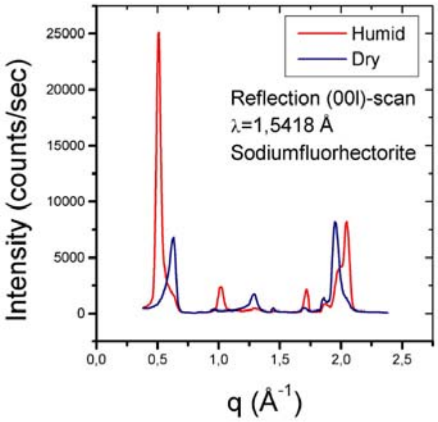

Figure 4.7: Previous figures in the same plot

### Potassium Fluorhectorite

The figures show a movement in the (001) posistion. The movement represents a dimension comparable with the dimension of one water molecule. I figure 4.9, an intermediate state is suggested for potassium fluorhectorite. It seems that water is partly intercalated in the sheet structure. A growing 002-peak is clearly at q=1,0 in figure 4.10.

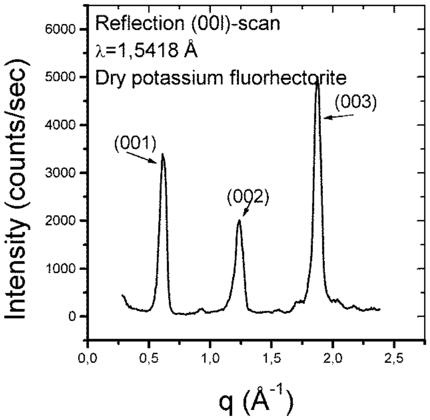

Figure 4.8: Potassium fluorhectorite at dry conditions

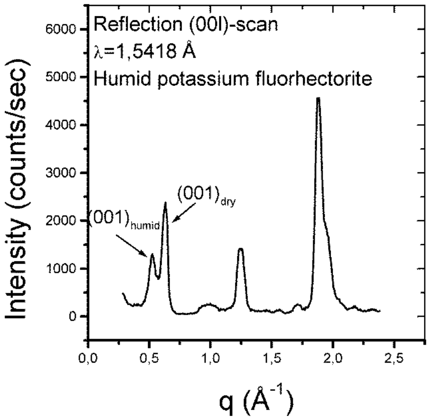

Figure 4.9: Potassium fluorhectorite at wet conditions

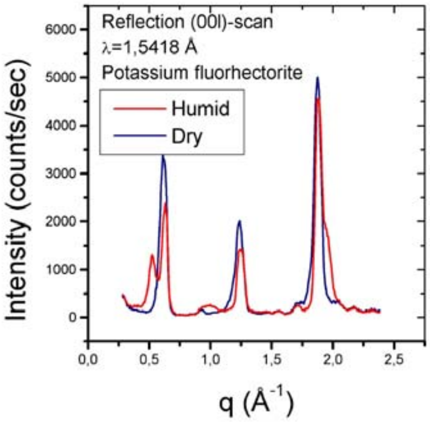

Figure 4.10: Previous figures in the same plot

### 4.1.2 Intensity simulations for total q range

The total intensity in the scattered signal is a product of three contributions, discussed in the theory chapter.

$$I(\theta) = [G^2(\theta)][\Phi(\theta)][L_p(\theta)] \tag{4.1}$$

The functions are all defined in the theory part. Substituting $\theta$ with $q$ makes it possible to simmulate different scattering patterns and find a set of parameters that fits the measured intensity. The G-factor is dependent on interlayer cation, but an approximation with the sum of three gaussians for trioctahedral silicates has been derived, based on findings in the literature [23]. By this simulation procedure, parameters for the three gaussians are found, and they are listed in a table for each ion. The width of the peaks is adjusted with the number of sheets N, in one crystallite. The amplitudes of the three gaussians reflect the G-factor for each ion.

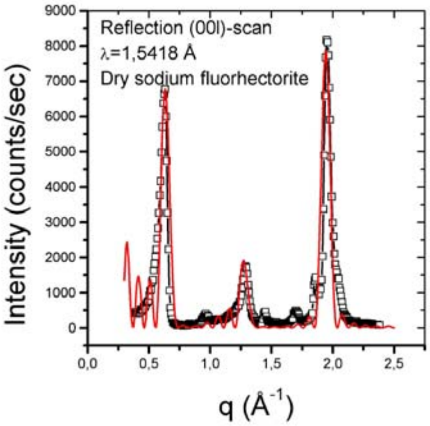

Figure 4.11: Simulated diffractionpattern for dry sodium fluorhectorite.

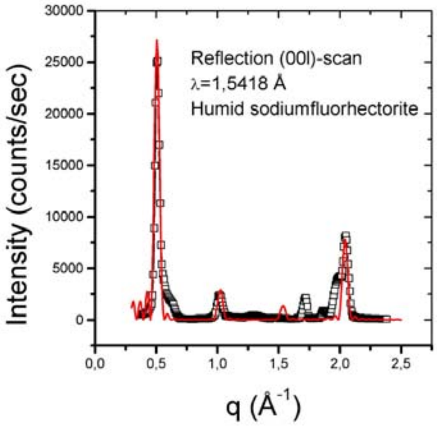

Figure 4.12: Simulated diffractionpattern for wet sodium fluorhectorite.

### Sodium Fluorhectorite

The simulated diffraction pattern for sodium fluorhectorite fits well with experimental data when the parameters in the total intensity function are the ones given in table 4.1.2

Table 4.1: Simulation parameters for Sodium fluorhectorite

| State | $A_1$ | $A_2$ | $A_3$ | $P_1$ | d-spacing | N (nr. of sheets) |
|---|---|---|---|---|---|---|
| Dry | 2,2 | 17 | 3,2 | 0,016 | 9,7 | 7 |
| Humid | 2,2 | 4 | 3,2 | 0,01 | 12,3 | 9 |

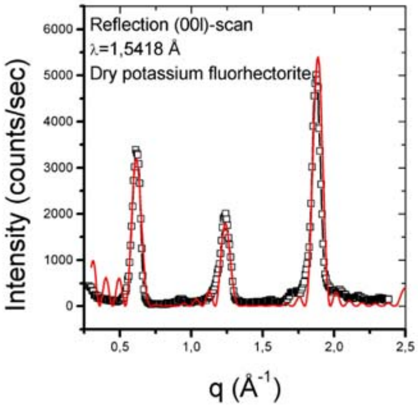

Figure 4.13: Simulated diffractionpattern for dry potassium fluorhectorite.

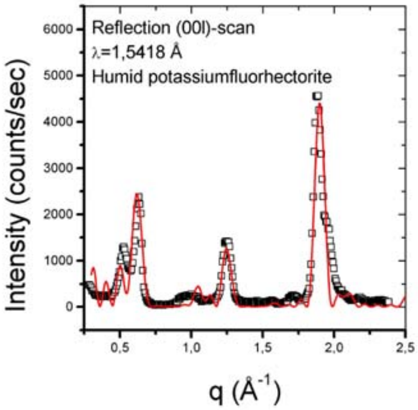

Figure 4.14: Simulated diffractionpattern for wet potassium fluorhectorite.

### Potassium Fluorhectorite

For the dry sample simulated diffraction pattern for potassium fluorhectorite agree well with the experimental data. Parameters in the total intensity function are given in the table.

Table 4.2: Simulation parameters for dry Potassium fluorhectorite

| State | $A_1$ | $A_2$ | $A_3$ | $P_1$ | d-spacing | N (nr. of sheets) |
|---|---|---|---|---|---|---|
| Dry | 1,8 | 18 | 5 | 0,0075 | 10 | 7 |

### Humid potassium fluorhectorite

For the humid potassium fluorhectorite, two d-spacings are proposed, and a satisfactory fit with the experimental data is obtained. Parameters are given in the table.

Table 4.3: Simulation parameters for humid Potassium fluorhectorite

| State | $A_1$ | $A_2$ | $A_3$ | $P_1$ | $P_2$ | $d_1$ | $d_2$ | $N_1$ | $N_2$ |
|---|---|---|---|---|---|---|---|---|---|
| Humid | 1,8 | 18 | 5 | 0,006 | 0,0005 | 9,93 | 12,0 | 7 | 6 |

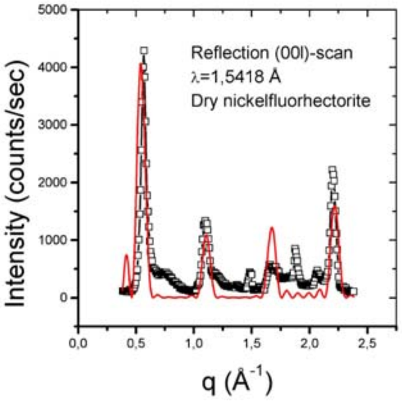

Figure 4.15: Simulated diffractionpattern for dry nickel fluorhectorite.

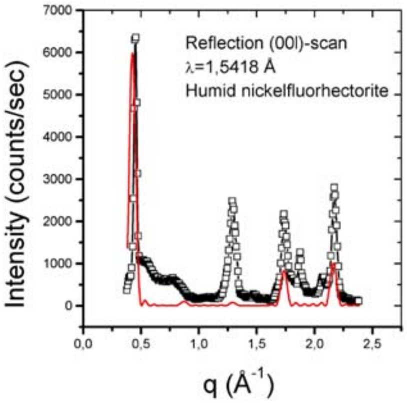

Figure 4.16: Simulated diffractionpattern for wet nickel fluorhectorite.

### Nickel Fluorhectorite

Simulated diffraction patterns for nickel fluorhectorite diverge the most from the experimental data. The parameters used are given in the table for the humid and for the dry situation. More work has to be done to get a proper fit between the experimental and the simulated diffraction patterns. Hendricks-Teller simulations were performed without any sucsess.

Table 4.4: Simulation parameters for Nickel fluorhectorite

| State | $A_1$ | $A_2$ | $A_3$ | $P_1$ | d-spacing | N (nr. of sheets) |
|---|---|---|---|---|---|---|
| Dry | 2,2 | 6 | 5 | 0,0025 | 11,3 | 6 |
| Humid | 2,2 | 6 | 5 | 0,0025 | 14,5 | 6 |

### 4.1.3 Dynamics of intercalation

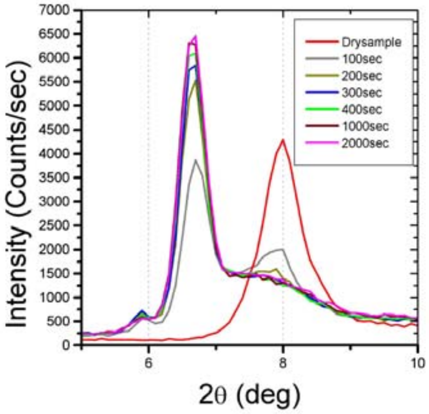

Figure 4.17: Dynamics of water intercalation in nickel fluorhectorite

**Nickel fluorhectorite**

A clay sample was kept at humid conditions of $RH = 97\%$ at $T = 25°C$ and a temperature $T = 80°C$. Then the temperature was lowered to $T = 60°C$ at constant humidity conditions. The 001-diffraction peak was plotted as a function of time and the result is given in figure 4.17. A further decrease in the temperature to $T = 40°C$ at constant humidity is shown in figure 4.18. The d-spacing increases a small amount, possibly due to arrangements of the intercalated water molecules. When the temperature drops from $T = 40°C$ to $T = 25°C$, the d-spacing has stabilized, giving a higher intensity in the signal as shown in figure 4.19.

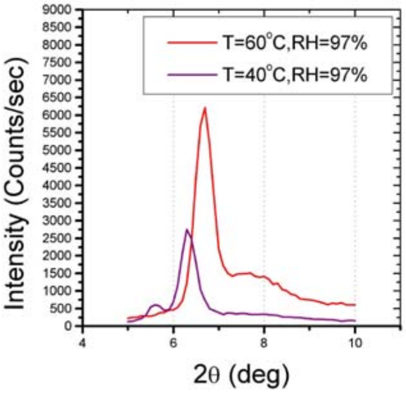

Figure 4.18: Dynamics of water intercalation in nickel fluorhectorite

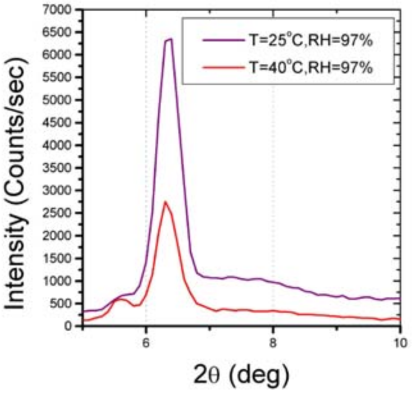

Figure 4.19: Dynamics of water intercalation in nickel fluorhectorite

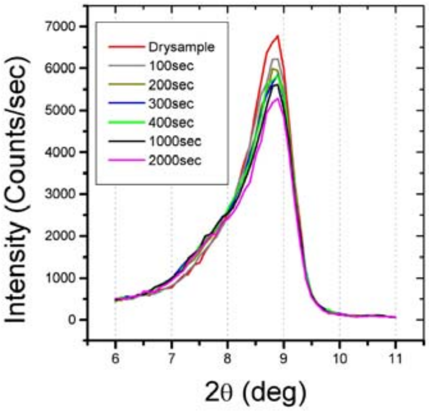

Figure 4.20: Dynamics of water intercalation in sodium fluorhectorite

## Sodium fluorhectorite

A sample of sodium exchanged fluorhectorite was exposed to the same sequence of conditions as the previous one. The results are shown in figure 4.20, in figure 4.21 and in figure 4.18. The transition between dry and wet sample occurs at another temperature for sodium than for nickel. One possible explanation of this puzzeling difference is found in an article by Zabat et al. [45]. It is presented after looking at the potassium samples.

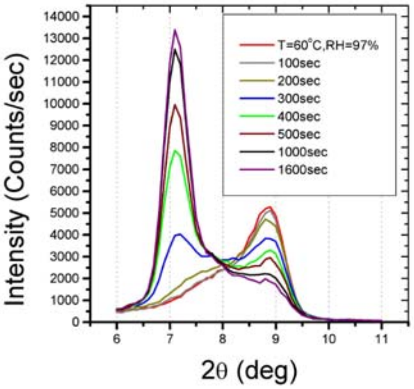

Figure 4.21: Dynamics of water intercalation in sodium fluorhectorite

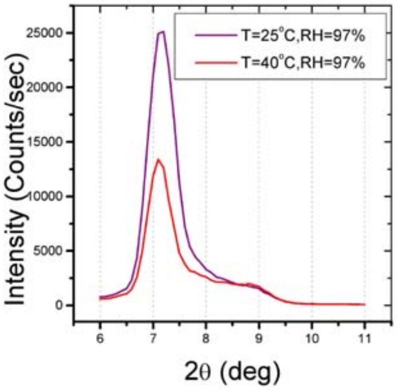

Figure 4.22: Dynamics of water intercalation in sodium fluorhectorite

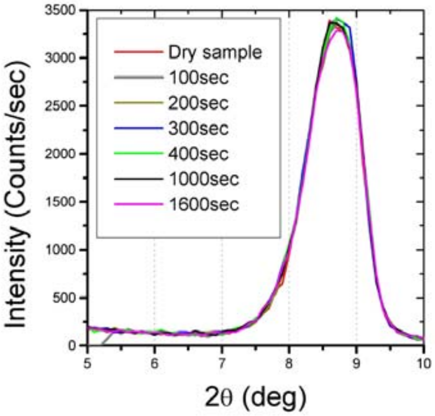

Figure 4.23: Dynamics of water intercalation in potassium fluorhectorite

### Potassium fluorhectorite

A sample of potassium exchanged fluorhectorite was exposed to the same sequence of conditions as the previous ones. The transition between dry and wet sample is not complete for this sample, even at the lowest temperature. Some stacks are intercalated with one layer of water, while others stay dry.

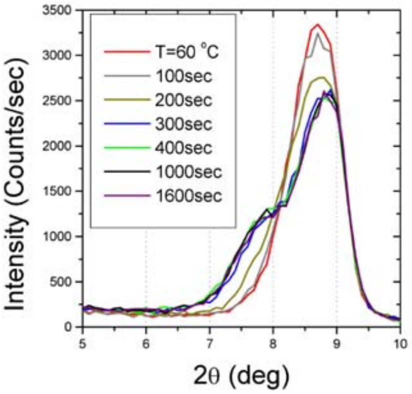

Figure 4.24: Dynamics of water intercalation in potassium fluorhectorite

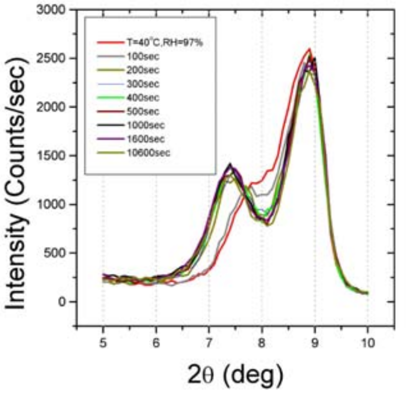

Figure 4.25: Dynamics of water intercalation in potassium fluorhectorite

### Possible cation-dependent dynamics

The microstructures and textures of smectite films are according to Zabat et al. [45] dependent on the interlayer cations. Divalent and trivalent cations are found to increase the local stacking order. Two extreme cases are described as entangled clays with monovalent cations on one hand and stacked clays with divalent ions on the other hand. The two different types are shown in figure 4.26. The more open texture of nickel exchanged fluorhectorite may influence and increase the accessibility of the clay particles for the watermolecules, at least on a macroscale. Another, and more likely, explanation may be the hydration energies involved for the different cations. Hydration energies are considerably higher for divalent ions than for monovalent ions, see [46] page 32. Furthermore the hydration energy for $Na^+$ is higher than for $K^+$.

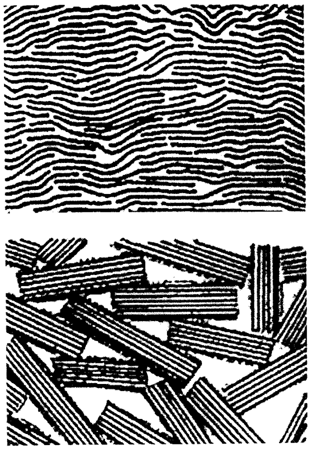

Figure 4.26: Entangled clay in the upper half. Stacked clay in the lower half.

## 4.1.4 Analysis of intercalation dynamics

The transition between the dry state and the humid state has been analysed by fitting two gaussians with fixed center positions in the peak fitting module of Origin. In the where two distinct peaks are present, like in figure 4.27, no fitting problems are encountered. However, when the system is in an intermediate state, like in figure 4.28, the gaussians do not fit properly. The reason may be that the swelling prosess is going while the $\theta - 2\theta$-scan is running. A Hendricks-Teller simulation has been done without any success to try to get a better fit with the dataset. The width and areas of the gaussians are given in following the table. The areas and widths of the peaks can be plotted as a function of time to see the developement in the water intercalation process. These curves are not presented here due to lack of time.

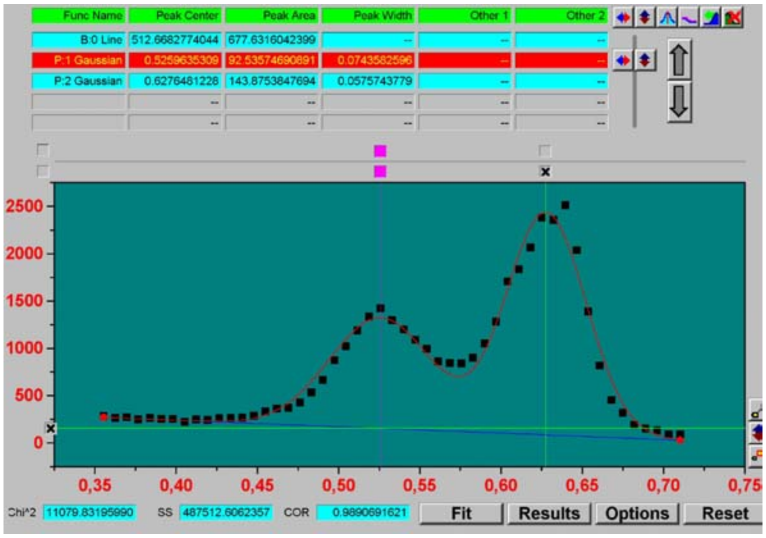

| Func Name | Peak Center | Peak Area | Peak Width | Other 1 | Other 2 |
|---|---|---|---|---|---|
| B:0 Line | 512.6682774044 | 677.6316042399 | -- | -- | -- |
| P:1 Gaussian | 0.5259635309 | 92.53574690891 | 0.0743582596 | -- | -- |
| P:2 Gaussian | 0.6276481228 | 143.8753847694 | 0.0575743779 | -- | -- |
|  | -- | -- | -- | -- | -- |
|  | -- | -- | -- | -- | -- |

Chi^2 11079.83195990 SS 487512.6062357 COR 0.9890691621

Figure 4.27: Fitting two gaussians to the intensity from potassium fluorhectorite

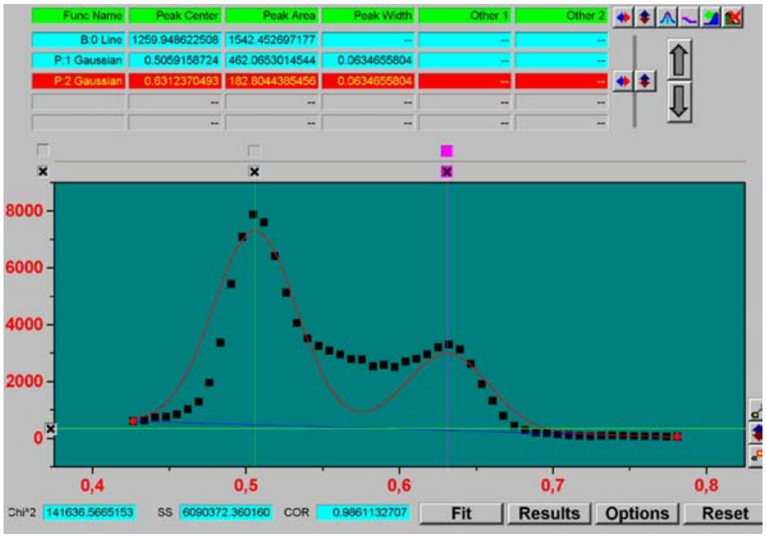

| Func Name | Peak Center | Peak Area | Peak Width | Other 1 | Other 2 |
|---|---|---|---|---|---|
| B:0 Line | 1259.948622508 | 1542.452697177 | -- | -- | -- |
| P:1 Gaussian | 0.5059158724 | 462.0653014544 | 0.0634655804 | -- | -- |
| P:2 Gaussian | 0.6312370493 | 182.8044385456 | 0.0634655804 | -- | -- |
|  | -- | -- | -- | -- | -- |
|  | -- | -- | -- | -- | -- |

Chi^2 141636.5665153 SS 6090372.360160 COR 0.9861132707

Figure 4.28: Fitting two gaussians to the intensity from sodium fluorhectorite

Table 4.5: Width W, and area A, of diffraction peaks as a function of time

| Sample | Time (sec) | W peak 1 | W peak 2 | A peak 1 | A peak 2 |
|---|---|---|---|---|---|
| Ni80to60 | 0 | - | 0,053 | - | 205 |
| | 100 | 0,036 | 0,078 | 122 | 122 |
| | 200 | 0,032 | 0,104 | 166 | 118 |
| | 300 | 0,031 | 0,118 | 172 | 125 |
| | 400 | 0,031 | 0,135 | 183 | 141 |
| | 500 | 0,031 | 0,126 | 189 | 131 |
| | 1000 | 0,031 | 0,145 | 195 | 151 |
| Na60to40 | 0 | 0,09 | 0,055 | 274 | 170 |
| | 100 | 0,096 | 0,052 | 243 | 194 |
| | 200 | 0,11 | 0,051 | 203 | 264 |
| | 300 | 0,063 | 0,070 | 273 | 331 |
| | 400 | 0,059 | 0,063 | 183 | 462 |
| | 500 | 0,059 | 0,059 | 148 | 551 |
| | 1000 | 0,058 | 0,058 | 132 | 709 |
| | 1600 | 0,055 | 0,055 | 129 | 718 |
| K40to25 | 0 | 0,094 | 0,048 | 119 | 107 |
| | 100 | 0,087 | 0,051 | 96 | 121 |
| | 200 | 0,079 | 0,054 | 94 | 135 |
| | 300 | 0,083 | 0,053 | 100 | 133 |
| | 400 | 0,080 | 0,054 | 100 | 134 |
| | 500 | 0,077 | 0,054 | 96 | 138 |
| | 1000 | 0,079 | 0,055 | 97 | 139 |

### 4.1.5 Rocking scan around (003)-peak

Rocking scans were performed around selected peaks for some samples. An intersting observation was done for the rocking scan around the (003) peak for $Na^+$-exchanged fluorhectorite. The curves are found in figure 4.29. The black curve represents a dry sample at 80°$C$ and $RH = 4\%$, whether the green curve represents a sample with one intercalated waterlayer at 40°$C$ and $RH = 76\%$. A dramatic change is observed for the intensity. For the wet sample, certain directions give considerably higher intensity. This pattern could be explained by a better internal alignement of the crystallites, or by the fact that the (003)-peak is “hidden” in the wet state. The dramatic loss in total intensity supports this explanation. Rocking scans should be done for all the samples and the width of the curve will reveal the details concerning changes in the crystallite alignements in the material while humidification.

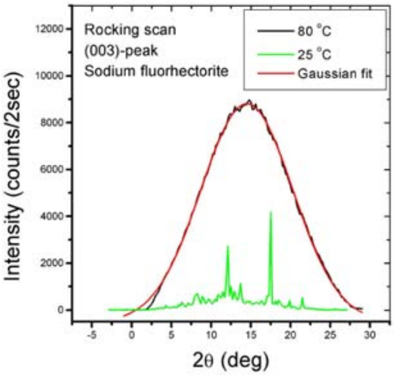

Figure 4.29: Rocking scan around (003)-peak.

Table 4.6: Parameters for Gaussian fit in Origin

| | | |
|---|---|---|
| Center | 14,50 | ±0, 01 |
| Width | 11,54 | ±0, 06 |
| Area | 13400 | ±1045 |

A gaussian fit is done to the dry sample, giving important values in table 4.6. All observations of this phenomenon in this work are similar to the one in figure 4.29.

## 4.2 Neutron scattering

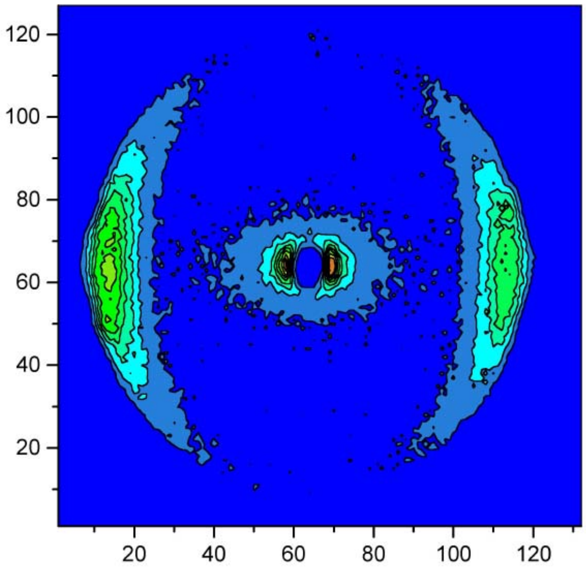

Figure 4.30: Dry nickel fluorhectorite

Figure 4.30 and figure 4.31 shows two 2D plots of the measured intensity of nickel fluorhectorite measured at a distance $2m$ from the sample with a wavelength of 3Å. The colours represent the same amount of counts in both figures. The center position is protected by a beam stop, giving an area of no intensity in the middle. Two factors should be noted in both figures. First, the center of the “half-moons” moves towards the center of the detector when the sample is wet. This diffraction effect is the same as seen in x-ray scattering. Secondly, the scattering is anisotropic, reflecting the anisotropy of the sample. Finally, it is seen that the small angle neutron scattering,

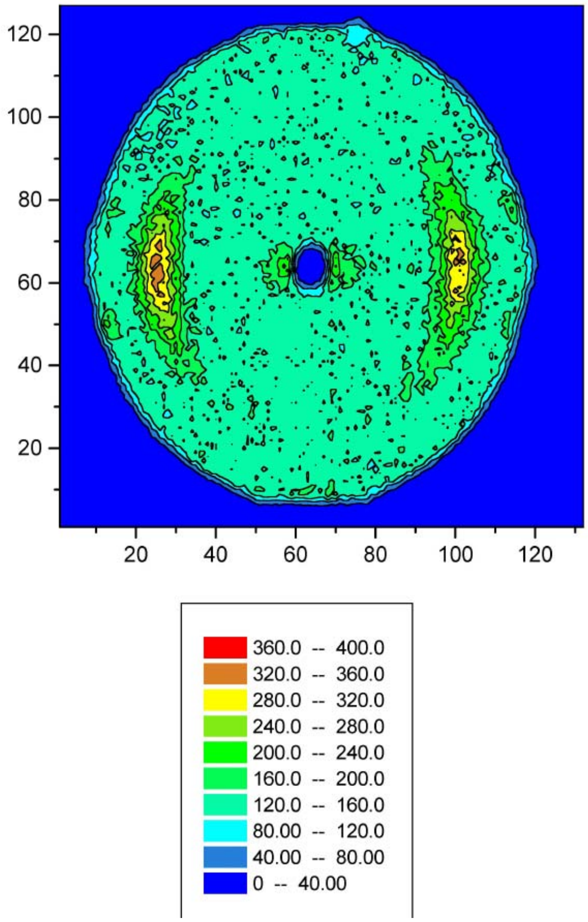

Figure 4.31: Nickel fluorhectorite in $D_2O$

next to the beamstop is also anisotropic. The small q values involved reflect anisotropic, characteristic dimensions in the sample on a higher lengthscale. The anisotropic property of the material beside the alignment of the clay platelets is most certainly cracks. Long cracks parallel with the particle alignment will influence the elastic properties of the material, and an effort to detect this is made by means of cw ultrasonics.

Neutrons are scattered both perpendicular to and parallel with the platelets as specified in figure 3.11. A plot of normalised data for all clay types in the dry state is given in figure 4.32 for the perpendicular direction and in figure 4.33 for the parallel direction. No peak is found in the perpendicular direction, while the peak is most clear for sodium and nickel type of clays.

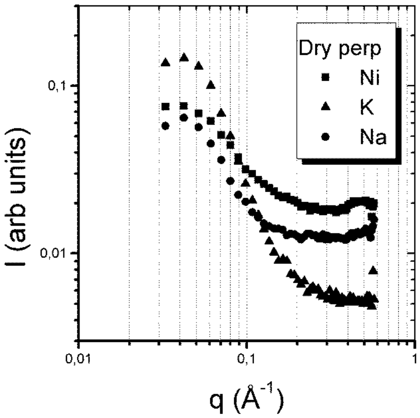

Figure 4.32: Neutron scattering perpendicular to particle alignement

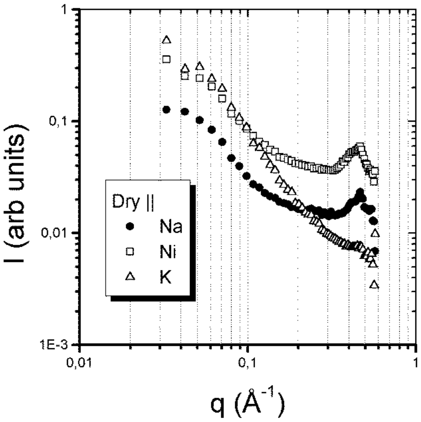

Figure 4.33: Neutron scattering parallel with particle alignement

Using the relation between the d-spacing and q, $d = \frac{2\pi}{q}$ gives a d-spacing of about 14 Å for "dry" samples. This is a higher value than the one found for dry samples by x-ray scattering. A possible explanation to this difference is found in the history of the samples. The cm-thick samples used for neutron scattering were dried at a temperature of $110°C$ for only 6 hours, while the mm-thick samples used for x-ray scattering were dried for more than 24 hours at the same temperature. Probably, the intercalated water in the neutron samples didn't have enough time to get out.

### 4.2.1 Clay powder diffraction

Clay powder with the three different ions were investigated in a wider q range than the aligned samples. Figure 4.34 shows the results of the scattering. A linear fit is made for the datasets, and a the different exponents are found in the figure. According to the theory chapter, the $\alpha$-exponent in the range

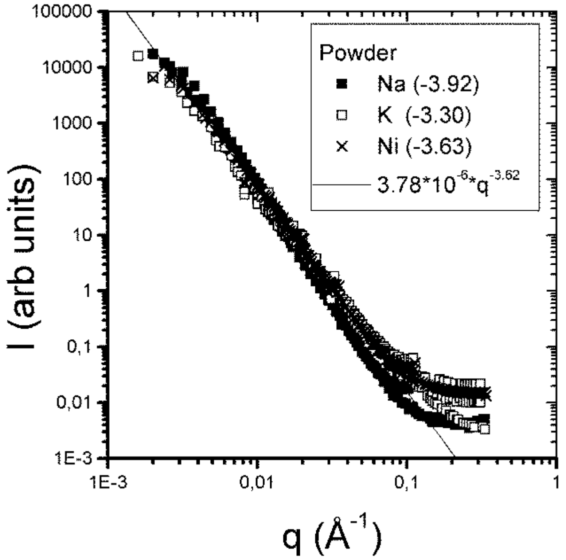

Figure 4.34: Small angle neutron scattering on fluorhectorite powder

of 3,3-3,9 represents a surface fractal. This observation is in good agreement with the findings of Lucido et al. [47] who have studied different volcanic rocks by means of small angle neutron scattering. Furthermore it is in agreement with the data obtained in the diploma thesis of Frøydis Rommundset by means of an atomic force microscope (AFM) [48]. A possible explanation of the different exponents for different ions could eg. be the ion radius, but more detailed studies must be done to draw such a conclusion.

## 4.3 Continous wave ultrasonics

The data registered during cw ultrasonics experiments were the mechanical resonant frequencies of the composite resonator and the swelling of the sample. Both datasets give valuable information about the material.

### 4.3.1 Swelling

Swelling of the sample was measured in the parallel and perpendicular direction for a dry sample exposed for a relative humidity of 97% at a temperature of T=25 °C. A uniaxial stress of about 520kPa was constantely applied during the swelling process. The dimensions of the sample in the direction of swelling is 2-3 mm. Hence, according to the LVDT calibration formula, the total expansion of the sample in the perpendicular direction is about $3-5\%$. The total signal measured over a period of 14 days is shown in figure 4.35. The minor oscillations in the signal has a period of 24 hours, and must be expained with the temperature fluctuations in the laboratory. However, in the first period of time, an obvious swelling takes place. This period is blown up in figure 4.36. As seen in the figure, it takes about two and a half hours for the sample to reach the first saturation. A similar swelling experiment was performed on another for only two days to see if the swelling was associated with the same time constant. The data are presented in figure 4.37. The sample reaches a first saturation or equilibrium after the same time as the previous one. However, a new swelling is initiated some hours later. This signal is not a result of a varying temperature in the laboratory and must have other explanations. Experiments have been done by x-ray diffraction to check whether water is intercalated in between the clay sheets at these conditions. No evidence of such an effect is prooven for the time being. Consequently, the swelling probably occurs when water molecules are absorbed in the pores of the material, suggested in the lower part of figure 4.38. More precise studies of this phenomenon must be carried out before any conclusion can be drawn. Another observation when it comes to swelling is that almost no swelling occurs in the parallel direction under the same conditions. This is shown in figure 4.39.

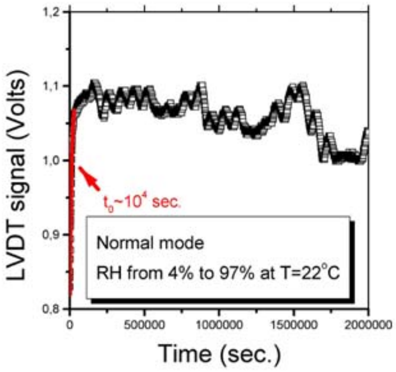

Figure 4.35: Swelling in perpendicular direction of nickel fluorhectorite for 14 days

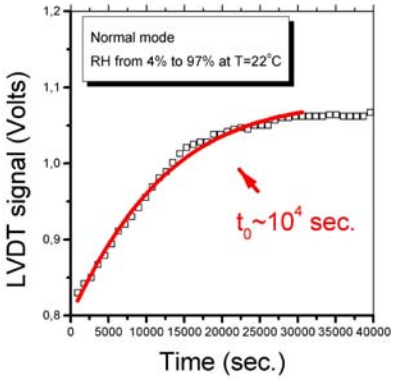

Figure 4.36: Swelling in perpendicular direction of nickel fluorhectorite

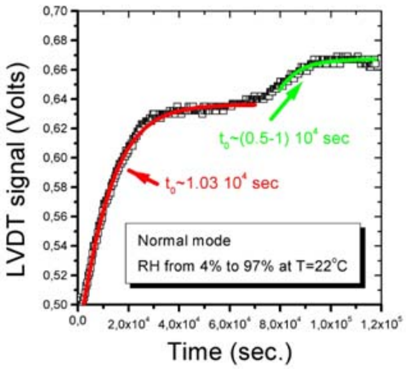

Figure 4.37: Swelling of dry nickel fluorhectorite at a relative humidity of 97% at $T = 25°$C

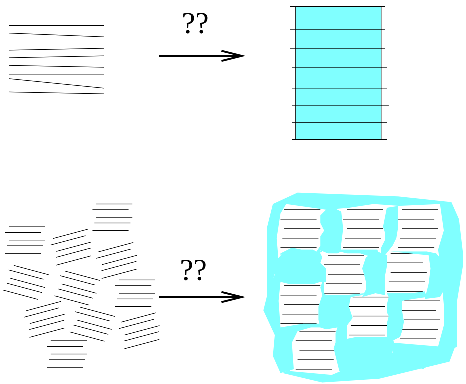

Figure 4.38: Two possible regimes of swelling for fluorhectorite

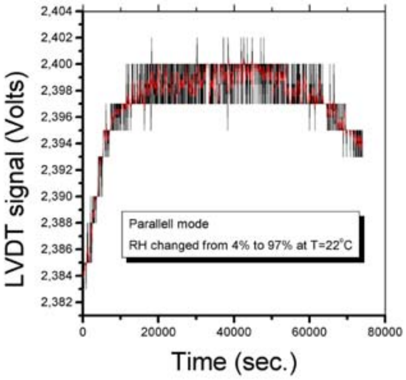

Figure 4.39: Swelling in parallel direction of nickel fluorhectorite

### 4.3.2 Wave propagation

Only p-wave measurements were done and analysed on nickel fluorhectorite samples due to lack of time. The wave propagation was measured in the parallel and the perpendicular direction of the particle alignment. Figure 4.40 shows a signal from a p-wave transducer with a center frequency of 5 MHz. To find the p-wave velocity we must pick the mechanical resonance peaks and find the distance between them. This can be done by finding the period of the signal by a simple Fast Fourier Transform (FFT) analysis in Origin. Picking the period from the raw signal an appropriate band pass filter is chosen, taking care of possible changes in the p-wave velocity. This filtered signal is run through an FFT and we get the characteristic frequency of the signal as a peak in the fourier spectrum shown in figure 4.41. Taking several measurements on the swelling clay, it is seen from figure 4.42 that a change in the p-wave velocity is reflected in the drift of the peak in the fourier spectrum. The velocities and effective bulk modulus can be plotted as a function of relative humidity in the air, and the plots are given in figure 4.43 and in figure 4.44. For both parallel and normal mode, the p-wave velocity seems to approach the velocity of water. This may be a coincidence, and should not be taken as a conclusion. The signals contain valuable information about scattering and damping in the material, but no time was found for such an analysis for the time being.

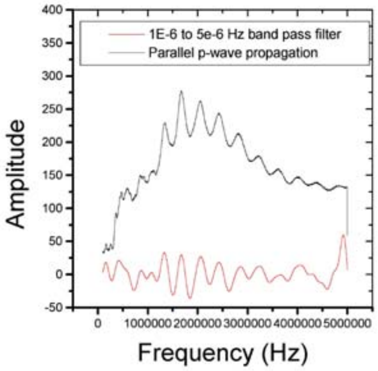

Figure 4.40: Ultrasound signal in parallel direction on dry nickel fluorhectorite

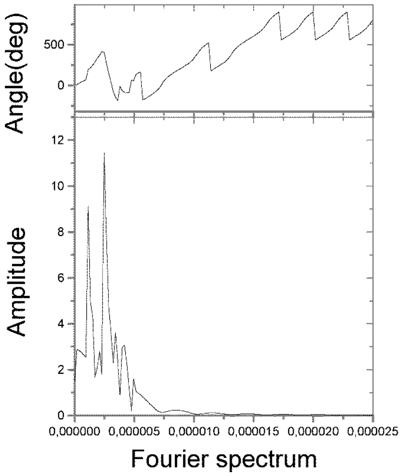

Figure 4.41: Fourier spectra of p-wave signal.

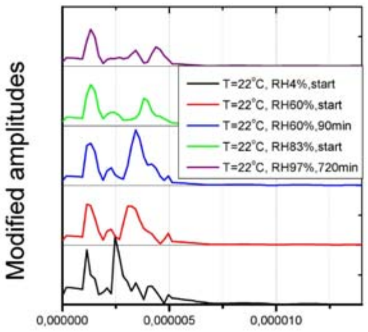

Figure 4.42: Fourier spectrum of the mechanical resonance frequencies in nickel fluorhectorite.

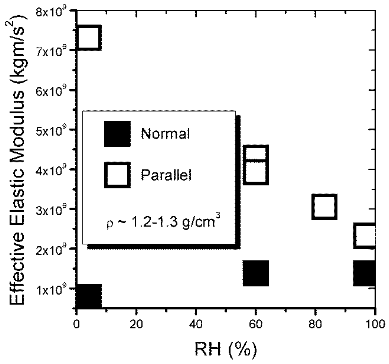

Figure 4.43: Bulk modulus of nickel fluorhectorite in parallel mode and in normal mode as a function of relative humidity

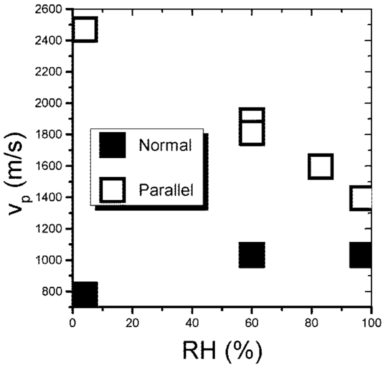

Figure 4.44: P-wave velocity in parallel direction and in normal direction of nickel fluorhectorite as a function of relative humidity

# Chapter 5

# Conclusion

Three different experimental techniques have been used to reveal information about the synthetic layered silicate fluorhectorite. Small Angle Neutron Scattering, X-ray diffraction and Continuous Wave ultrasonics all seem to provide valuable data for an understanding of the intercalation process of water in the sheet structure of the material. However, the total amount of work required to acquire and analyse all the data properly within the time limit of four months surpasses my capacity. Nevertheless, some preliminary conclusions can be drawn from the observations in the laboratory:

- Water is intercalated in the sheet structure of all the three types of fluorhectorite analysed in this study.
- The dynamics of the intercalation is most probably dependent on the interlayer cation.
- Rocking scans indicate a possible better alignment of the clay crystallites when water is intercalated.
- The procedure of making thick, dry, anisotropic, macroscopic, shalelike clay samples is successful.
- Small Angle Neutron Scattering gives an expected diffraction peak in one direction, and the powder analysis indicates a self-similar surface fractal $D$ in the range of $2,1 < D < 2,7$.
- P-wave velocity in the material is highly dependent on the direction of propagation, and an increase in humidity gives a decrease in the parallel wave velocity.
- Swelling is observed in the normal direction but not in the parallel direction when increasing the humidity in the air to RH=97% at T=25°. However, this swelling is not observed as an intercalation phenomenon and could be the result of water entering in between the crystallites.

### Further work suggested

For a better understanding of the dynamics of intercalation of water in fluorhectorite, nuclear magnetic resonance (NMR) and profilometry would be appropriate techniques to try out. NMR-investigation of layered silicate systems is a well established technique, and such complementary information about the dynamics of water would help us to draw further conclusions. To find the pore size distribution of the samples, cryoporometry is an interesting and possible technique on this system [49]. Profilometry is a technique that allows roughness measurements on surfaces while intercalation of water is happening. The technique would also be complementary to the previous used in this study. Furthermore, Small Angle Neutron Scattering should be performed on the clay samples in a wider q-range in order to investigate the pore surfaces more properly.

# Appendix A

# LVDT transducers

Instrumentation and LVDT-transducers delivered by RPD Electronics, Grove Street, Heath Town, Wolverhampton, WV10 0PY, UK.
The transducer number, type and their serial RDP-number are listed in table A. The signal -amplifier, -modulator and -monitor represent the Modular-600system.

Table A.1: LVDT transducers

| Transducer No. | Type | RDP No. |
|---|---|---|
| 1 | GTX 2500 | 4528 |
| 2 | GTX 2500 | 4533 |
| 3 | GTX 2500 | 4551 |

# Appendix B

# Number of interlayer cations

To have an idea of how many interlayer cations there are to be exchanged in one gram of fluorhectorite, I make use of the following assumptions:

- Density of clay sheet,[1] $\rho \approx 2.8\frac{g}{cm^3}$
- Surface charge,[2] $\sigma \approx 1.2e^-$ pr. unit cell
- Volume of unit cell,[3] $V \approx (10\text{Å})^3$
- Radius of clay sheet,[4] $r \approx 0.2\mu m$
- Height of one sheet,[5] $h = 10$ Å

Further derivation is now simple and straight forward. First, we find the number of clay sheets, $N$, in one gram of clay:

$$V = \frac{m}{\rho} \Rightarrow N\pi r^2 h = \frac{m}{\rho} \tag{B.1}$$

With proper insertion of the given numbers, we will find:

$$N = 2.8 * 10^{18} platelets \tag{B.2}$$

Using this number, we can calculate the appropriate amount of salt needed to exchange the interlayer cations. In this study, 50 times as many saltions as origin cations were added to the solution.

---

[1] From Kaviratna [7]

[2] From Kaviratna [7]

[3] From Laponite Bulletin [50]

[4] From Kaviratna [7]

[5] From Laponite Bulletin [50]

# Bibliography

[1] F. Levy (ed.) *Physics and Chemistry of Materials with Layered Structures.* Reidel, Dordrecht, 1979

[2] R. Garcia et al. *Clay materials from antique pottery.* Thermochimica Acta, 303 (1997).

[3] M. M. Molenaar et al. *A constitutive model for swelling shales.* SPE/ISRM 47332, 1998.

[4] R. J. F. Leote de Carvalho et al. *Non-linear Poisson-Boltzmann theory for swollen clays.* Europhysics Letters, **43** (4), pp.369-375 (1998).

[5] J. D. Sherwood & H. van Damme *Nonlinear compaction of an assembly of highly deformable platelike particles.* Physical Review E, Volume 50, Number 5, November 1994.

[6] Z. P. Zhang et al. *Analysis of the Pore Characteristics of Mixtures of Disks.* Journal of Colloid and Interface Science, 195, 8-18 (1997).

[7] P. D. Kaviratna et al. *Dielectric Properties of Smectite Clays.* J. Phys. Chem. Solids, Vol. 57, No. 12, 1996, 1897-1906.

[8] N. Wada et al. *X-ray-diffraction studies of hydration transitions in Na vermiculite.* Physical Review B, Volume 41, Number 18, The American Physical Society, 1990, 12895-12901.

[9] S. A. Solin *The structure, morphology and layer rigidity of clay intercalation compounds.* Chemical Physics of Intercalation II, ed. P. Bernier et al., Plenum Press, New York 1993.

[10] S. A. Solin , J. Mol. Catalysis 27, 293, 1984

[11] R. E. Grim *Clay Mineralogy*, McGraw-Hill New York, 1968

[12] Y. Cai et al. *Rigidity of randomly intercalated layered solids. II. Gallery structure of multilayers.* Physical Review B, Volume 42, Number 14, November 1990.

[13] B. Velde *Introduction to Clay Minerals – Chemistry, Origins, Uses And Environmental Significance.* Chapman & Hall, 1992.

[14] H. van Olphen *An Introduction to Clay Colloid Chemistry– Second edition.* Krieger Publishing Company, Malabar, Florida, 1991.

[15] Jacob Israelachvili *Intermolecular & Surface Forces – Second edition.* Academic Press Limited, 1992.

[16] S. Lee & S. A. Solin *X-ray study of the intercalant distribution in mixed alkyl ammonium pillared clay.* Physical Review B, Volume 43, Number 14, 1991.

[17] Jean-Cristophe P. Gabriel et al. *Observation of Nematic Liquid-Crystal Textures in Aqueous Gels of Smectite Clays.* J. Phys. Chem. 1996, 100, 11139-11143. American Chemical Society.

[18] Stephen W. Lovesey *Theory of Neutron Scattering from Condensed Matter - Volume 1.* Oxford Science Publications, Clarendon Press, Oxford.

[19] Mikkelsen, Elgeseter & Stokke *Molecular Biophysics.* NOBIPOLs forskningsstiftelse, Trondheim.

[20] H. P. Klug & L. E. Alexander *X-ray diffraction procedures - Second edition.* John Wiley & Sons, New York

[21] Duane M. Moore & Robert C. Reynolds, Jr.*X-Ray Diffraction and the Identification and Analysis of Clay Minerals* Chapter 3, pages 57-101, Oxford University Press 1989

[22] W. F. Cole et al. *Tabular data of layer structure factors for clay minerals.* Acta Cryst. 21, p. 836, 1966

[23] G. W. Brindley & G. Brown ed. *Crystal structures of clay minerals and their X-ray identification.* Mineralogical society, p. 257, 1980.

[24] D. Avnir et al. , Nature (London) 308, 261, 1984

[25] A. J. Katz & A. H. Thompson, Phy Rev. Lett. 54, 1325, 1985

[26] John C. Bailar et al. *Chemistry - Third edition.* Harcourt Brace Jovanovich, Publishers, Academic press, p. 307-310, 1989.

[27] Po-zen Wong & James Howard & Jar-Shyong Lin *Surface Roughening and the Fractal Nature of Rocks.* Physical Review Letters, Volume 57, Number 5, August 1986.

[28] P. Debye et al, Journ. Appl. Phys. 28, 679, 1957

[29] D. W. Schaefer & K. D. Keefer, Phys. Rev. Lett. 53, 1383, 1984

[30] P.-z Wong, Phys. Rev. B 32, 7417, 1985

[31] H. D. Bale & P. W. Schmidt, Phys Rev. Lett. 53, 596, 1984

[32] W. P. Mason, "Physical Acoustics" (W. P. Mason, ed.), VolIA, Chapter 5, Academic Press, New York.

[33] H. J. McSkimin, J. Acoust. Soc. Am. 37, 864

[34] C. Jin *A continous wave method for simultaneous sound velocity and attenuation measurements.* Rev. Sci. Instrum. 67 (1), January 1996.

[35] E. D. Brandner et al. *Damping capacity of layered materials.* Journal of Applied Physics 76 (12), 15 December 1994.

[36] L. E. McNeil & M Grimsditch *Elastic moduli of muscovite mica.* J. Phys: Condensed Matter 5, (1993), 1681-1690.

[37] Odd Arild Olsen *Instrumenteringsteknikk.* Tapir Forlag, p. 241, 1994

[38] Simen Berg Lutnæs *Forberedelser til akustiske målinger på leire.* Project 1998, Department of Physics, NTNU.

[39] D. W. Thompson & J. T. Butterworth *The Nature of Laponite and Its Dispersions.* Journal of Colloid and Interface Science, Vol. 151, No. 1, June 1992.

[40] A. Mourchid & P. Levitz *Long-term gelation of laponite aqueous dispersions.* Physical Review E, Volume 57, Number 5, May 1998.

[41] John D. F. Ramsay et al. *Swelling and Dispersions of Smectite Clay Colloids: Determination of Structure by Neutron Diffraction and Small-angle Neutron Scattering.* J. Chem. Soc. Faraday Trans., 1990, 86(23), 3919-3926.

[42] Mason & Thurston *Physical Acoustics VIII – Principles and Methods.* Academic Press, 1971.

[43] Olav Magnar Nes, Rune Martin Holt et al. *Rig-site and Laboratory use of CWT Acoustic Velocity Measurements on Cuttings.* Society of Petroleum Engineers, SPE 36854, 1996.

[44] Emil J. Samuelsen *X-ray diffractometer LØFTE.* Description of x-ray diffractometer used in this study. NTNU.

[45] M. Zabat et al. *Surface topography and mechanical properties of smectite films.* Progr. Colloid Polym. Sci (1997) 105, Steinkopff Verlag 1997.

[46] N. Güven & R. M. Pollastro *Clay-Water Interface and its Rheological Implications*. CMS workshop lectures, The Clay Minerals Society, Volume 4, 1992.

[47] G. Lucido et al. *Fractal approach in petrology: Small angle neutron scattering experiments with volcanic rocks*. Physical Review B, Volume 38, Number 13, 1988.CWprinsipp

[48] Frøydis Rommundset *AFM studies of deposited laponite clay surfaces.* Diploma work, NTNU, Trondheim, 1999

[49] S. G. Allen et al. *Internal surfaces of porous media studied by nuclear magnetic resonance cryoporometry*. Journal of Chemical Physics, Volume 108, Number 19, 15 May 1998.

[50] Laporte Absorbents *Laponite Technical Bulletin L 104/90/A*.